

CHAPTER

1

FUNDAMENTALS OF X-RAY FLUORESCENCE

1.1 A Short History of XRF	2
1.2 The New Variant TXRF	8
1.2.1 Retrospect on its Development	8
1.2.2 Relationship of XRF and TXRF	13
1.3 Nature and Production of X-Rays	15
1.3.1 The Nature of X-Rays	15
1.3.2 X-Ray Tubes as X-Ray Sources	17
1.3.3 Polarization of X-Rays	29
1.3.4 Synchrotron Radiation as X-Ray Source	30
1.4 Attenuation of X-Rays	44
1.4.1 Photoelectric Absorption	46
1.4.2 X-Ray Scatter	49
1.4.3 Total Attenuation	51
1.5 Deflection of X-Rays	53
1.5.1 Reflection and Refraction	53
1.5.2 Diffraction and Bragg's Law	59
1.5.3 Total External Reflection	62
1.5.4 Refraction and Dispersion	71

X-ray fluorescence (XRF) is based on the irradiation of a sample by a primary X-ray beam. The individual atoms hereby excited emit secondary X-rays that can be detected and recorded in a spectrum. The spectral lines or peaks of such a spectrum are similar to a bar-code and are characteristic of the individual atoms, that is, of the respective elements in the sample. By reading a spectrum, the elemental composition of the sample becomes obvious.

Such an XRF analysis reaches near-surface layers of only about 100 μm thickness but generally is performed without any consumption of the sample. The method is fast and can be applied universally to a great variety of samples. Solids can be analyzed directly with no or only little sample preparation. Apart from the light elements, all elements with atomic numbers greater than 11 (possibly greater than 5) can be detected. The method is sensitive down to the microgram-per-gram level, and the results are precise and also accurate if matrix-effects can be corrected.

For these merits, XRF has become a well-known method of spectrochemical analysis. It plays an important role in the industrial production of materials, in prospecting mineral resources, and also in environmental monitoring. The number of spectrometers in use is estimated to be about 15 000 worldwide. Of these, 80% are working in the wavelength-dispersive mode with analyzing crystals; only 20% operate in the energy-dispersive mode, mainly with Si(Li) detectors, and recently with Si-drift detectors. At present, however, energy-dispersive spectrometers are four times more frequently built than wavelength-dispersive instruments due to the advantage the former provides in fast registration of the total spectrum.

A spectrum originally means a band of colors formed by a beam of light as seen in a rainbow. The Latin word “spectrum” means “image” or “apparition.” The term was defined scientifically as a record of intensity dependent on the wavelength of any type of electromagnetic radiation. The “intensity” is to be interpreted as a number of photons with particular photon energy. Today, a spectrum can also be a record of a number of ions according to their atomic mass or it can demonstrate the number of electrons in dependence of their electron energy. The visual or photographic observation of such a spectrum is called *spectroscopy*. The term is deduced from the Greek verb “σκοπειν,” which means “to observe” or “to look at.” On the other hand, “μετρω” in Greek means “to measure” so that *spectrometry* is a quantitative photoelectric examination of a spectrum.

1.1 A SHORT HISTORY OF XRF

The foundations of spectrochemical analysis were laid by R.W. Bunsen, a chemist, and G.R. Kirchhoff, a physicist. In 1859, they vaporized a salt in a flame and determined some alkaline and alkaline-earth metals by means of an optical spectroscope. Today, optical atomic spectroscopy has developed a variety of new analytical techniques with high efficiency, such as atomic absorption spectroscopy (AAS) with flames (FAAS) or electrothermal furnaces (ET-AAS), and the inductively coupled plasma technique (ICP) combined with atomic emission or mass spectrometry (ICP-AES and ICP-MS). These techniques do entail some consumption of the sample, but they are highly suitable for ultratrace analyses of solutions.

Nearly 40 years after the discovery by Bunsen and Kirchhoff, in 1895, Wilhelm Conrad Röntgen (Figure 1.1) discovered a remarkable, invisible, and still unknown radiation, which he called X-rays. This name has been adopted in the English-speaking areas; only in German-speaking parts is the radiation called “Röntgenstrahlen” in his honor [1]. In 1901, Röntgen was awarded the first Nobel Prize in Physics. The great potential of X-rays for diagnostic purposes in medicine and dentistry was immediately recognized worldwide. Furthermore, different researchers clarified the fundamentals of X-ray spectroscopy and developed the methods of XRF (X-ray fluorescence) and XRD



Figure 1.1. Wilhelm Conrad Röntgen in 1895 (reproduced with permission of the “Deutsches Röntgenmuseum” in Lennep, Germany).

(X-ray diffraction) applicable to material analysis. Table 1.1 enumerates well-known and renowned scientists. Most of them came from Great Britain and Germany and almost all of them won the Nobel Prize in physics.

Hendrik Lorentz found the dispersion of X-rays and studied the influence of magnetic fields on rapidly moving charged particles by the “Lorentz force,” which 50 years later has built the basis for beamlines at synchrotron facilities. Lord Rayleigh detected the coherent scattering of X-rays, and Philipp Lenard investigated cathode rays while Sir J.J. Thomson verified them as negatively charged electrons. Lord Ernest Rutherford created his well-known model of atoms containing a positive nucleus and several negative electrons. Max von Laue, Friedrich, and Knipping showed the diffraction of X-rays by the lattice of crystalline copper sulfate [2] and hereby proved both the wave nature of X-rays and simultaneously the atomic structure of crystals.

In 1913, Sir William Henry and William Lawrence Bragg—father and son—built the first X-ray spectroscope as demonstrated in Figure 1.2 [3,4]. It consisted of a cathode-ray tube with a Mo anode, a goniometer with a revolving rock-salt crystal in the center, and a photographic film on the inside wall of a

TABLE 1.1. Important Scientists, Mostly Nobel Laureates who Established the Fundamentals of XRF and TXRF

Scientist	Country	Life	Research or Discovery	Nobel Prize
Wilhelm-Conrad Röntgen	Germany	1845–1923	Detection of Novel Invisible Rays	1901
Hendrik Antoon Lorentz	The Netherlands	1853–1928	Lorentz Force, Time Dilation; Dispersion	1902
Lord John William Strutt Rayleigh	United Kingdom	1842–1919	Coherent Scattering of X-rays; Gas Densities	1904
Philipp Lenard	Germany (Austria/Hungary)	1862–1947	Discharges in Cathode Ray Tubes	1905
Sir Joseph John Thomson	United Kingdom	1856–1940	Electrical Conductivity of Gases; the Electron	1906
Lord Ernest Rutherford	New Zealand, UK	1871–1937	Radioactivity; Rutherford's Modell of Atoms	1908
Max von Laue	Germany	1879–1960	Diffraction of X-rays by Crystals	1914
Sir William Henry Bragg , sen	United Kingdom	1862–1942	Determination of Crystal Structures by X-Rays	1915
William Lawrence Bragg , jun.	United Kingdom	1890–1971	Bragg's Law: $m\lambda = 2d \cdot \sin \theta$	1915
Henry Moseley	United Kingdom	1887–1915	Moseley's Law: $E = k \cdot (Z - \sigma)^2$	–
Charles Glover Barkla	United Kingdom	1877–1944	Characteristic X-rays of Elements; Polarization	1917
Max Planck	Germany	1858–1947	Energy Quanta or Photons	1918
Albert Einstein	Germany	1879–1955	Photoelectric Effect; Theory of Relativity	1921
Niels Bohr	Denmark	1885–1962	Atomic Structure examined by Radiation	1922
Karl Manne Georg Siegbahn	Sweden	1886–1978	X-ray spectroscopy; M series	1924
Arthur Holly Compton	United States of America	1892–1962	Incoherent Scattering; Total-Reflection of X-Rays	1927
Peter Debye	The Netherlands	1884–1966	Powder Diffractometry by X-Rays	1936
Kai Manne Börje Siegbahn	Sweden	1918–2007	X-ray Photo-electron Spectroscopy	1981

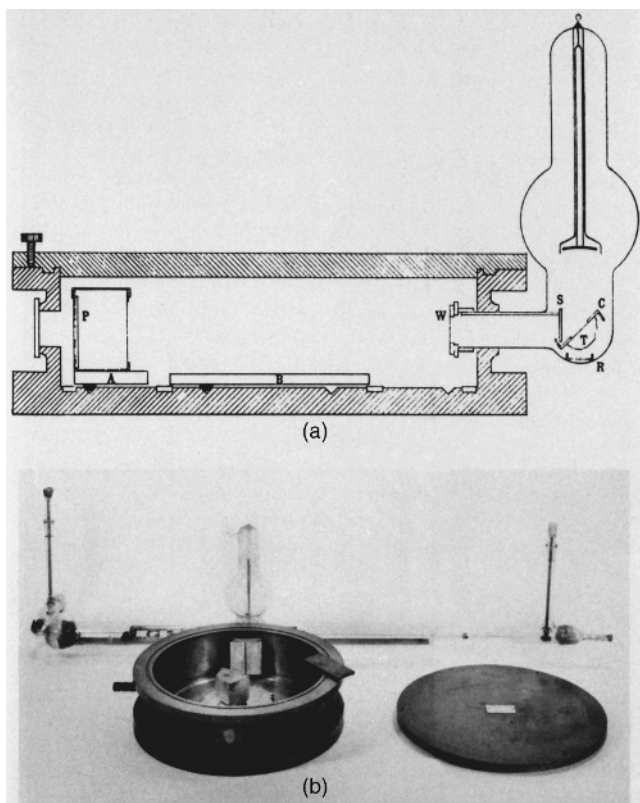


Figure 1.2. First X-ray spectroscopy used by Moseley in 1913. (a) X-ray tube with T = metal target that can be exchanged; S = slit; W = window; goniometer with B = base for the crystal; P = photographic film. (b) A metal cylinder in front of an X-ray tube. The cylinder with slit and rotating crystal in its center can be evacuated. Figure from Ref. [3], reproduced with permission from Taylor & Francis.

metallic cylinder. The Braggs explained the diffraction of X-rays at the three-dimensional crystal as their reflection at parallel planes of the crystal lattice and determined the wavelength of the X-radiation according to the law later called Bragg's law. Furthermore, the interplanar distance of different other crystals had been determined. Then, in 1913, Moseley established the basis of X-ray fluorescence analysis by replacing the Mo anode by several other metal plates. He found his well-known law [3], which relates the reciprocal wavelength $1/\lambda$ of the "characteristic" X-rays to the atomic number Z of the elements causing this radiation. Moseley probably missed a Nobel Prize because he was killed during World War I at the Dardanelles near Gallipoli when he was just 28 years old (Figure 1.3b).

In 1904, Barkla had already discovered the polarization of X-rays, which is a hint to their wavelike nature [5]. Ten years later, he bombarded metals with

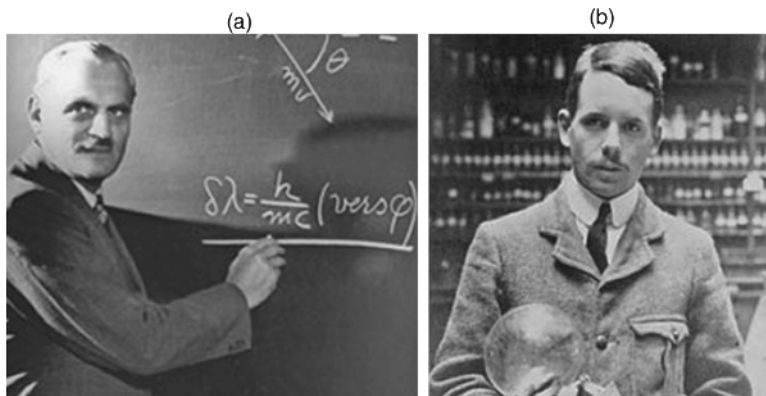


Figure 1.3. (a) Arthur Holly Compton in 1927 deriving his famous formula. Photo is from the public domain, © is expired. (b) Henry Moseley with an X-ray tube in 1913. Photo is from the public domain, © is expired.

electrons, which led to the emission of X-rays as “primary” radiation. Barkla excited the materials by this primary X-rays and together with Sadler he found their characteristic X-rays as “secondary” radiation [6]. He showed that the elemental composition of a sample could be examined by X-radiation and was awarded the Nobel Prize in 1917.

In contrast to the wavelike nature, Max Planck recognized the corpuscular nature of X-rays appearing as photons and Albert Einstein explained the photoelectric effect by means of such photons. Niels Bohr depicted the model of atoms consisting of a heavy nucleus with several protons and with an outer shell containing the same number of electrons. These electrons were assumed to revolve around the nucleus on several distinct orbits. The periodic system of the elements was discovered by Dimitri Mendelejew and Lothar Meyer in 1869. The naturally existing elements ordered with increasing atomic mass had got the place numbers $Z=1$ for hydrogen (the lightest element) up to $Z=92$ for uranium (the heaviest element). It could be explained now that Z is not an arbitrary number but the number of protons in the nucleus and the number of electrons in the outer shells of an atom. And the three anomalies of potassium, nickel, and iodine could be cleared up by the different atomic mass of their isotopes. Furthermore, six new elements could be predicted and had indeed been discovered in the next 20 years: the rare elements technetium, hafnium, rhenium, astatine, francium, and promethium.

Manne Siegbahn got the Nobel Prize for his discoveries of X-ray spectra. He determined the wavelength of characteristic X-rays with high accuracy by their diffraction at mechanically carved gratings under grazing incidence [1]. Arthur Holly Compton detected the incoherent scattering of X-rays. In 1923, he also discovered the phenomenon of external total reflection for X-rays [7]. He

found that the reflectivity of a flat target strongly increased below a critical angle of only about 0.1° . In 1927, Compton was awarded the Nobel Prize in Physics (Figure 1.3a). Ten years later, Debye won the Prize in chemistry for his investigation of X-ray powder diffractometry. And finally, Kay Siegbahn, son of Manne Siegbahn, received the Noble Prize for the discovery of X-ray photoelectron spectroscopy in 1981.

The years of fundamental discoveries were gone now and the time of industrial applications began. Already in 1924, Siemens & Halske (Germany) had built the first commercially available X-ray spectrometer with an open X-ray tube, revolving crystal, and photographic plate. Coolidge developed a vacuum-sealed cathode-ray tube as shown in Figure 1.4. Samples could easily be excited now by X-rays instead of electrons. Soller built a collimator consisting of several parallel metal sheets just right for the collimation of a broad X-ray beam. In the 1930s, Geiger and Müller developed a gas-filled photoelectric detector, which allowed for direct pulse-counting instead of a complicated development of the photographic plate. This detector was replaced by a gas-filled proportional detector and by a scintillation counter in the 1940s. Simultaneously, different analyzer crystals were produced with various spacings and high reflectivity, for example, lithium fluoride and pentaerythritol.

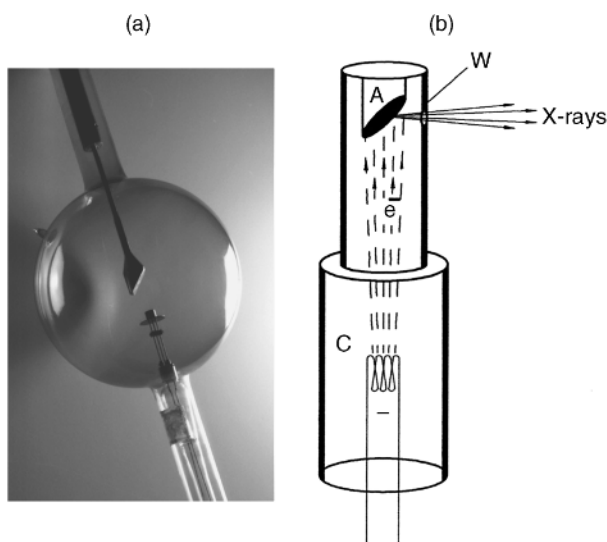


Figure 1.4. X-ray tube of the Coolidge type used as an X-ray photon source. (a) The vacuum-sealed glass bulb is an engineering marvel of glass blowing workshops from 1905. Photo of the authors, reproduced with permission from “Deutsches Röntgenmuseum,” Lennep, Germany. (b) Sketch of today’s X-ray tubes consisting of a metal–glass cylinder. C = tungsten-filament used as the cathode; A = metal block with a slant plane used as the anode; W = thin exit window. Figure from Ref. [8], reproduced with permission. Copyright © 1996, John Wiley and Sons.

After World War II, the first complete X-ray spectrometers became available, developed for example, by Philips, The Netherlands, by Siemens, Germany, and by ARL, Switzerland. In the 1960s, the spectrometers were equipped with hardwired controllers, servo transmitters, switching circuits, and electronic registration [4]. In the 1970s, X-ray spectrometers became computer-controlled and automated for a high throughput of samples. They were used for production and quality control in several branches of the metallurgical industry. Furthermore, X-ray spectrometers were applied in the exploitation of mineral resources and also in environmental protection. At this time XRF-spectrometers filled a whole lab, but in the 1980s the lateral dimensions decreased. In the decades since, XRF has developed into a powerful method of spectrochemical analysis of materials. However, classical XRF is not suitable for ultratrace analyses and it is notorious for producing matrix effects that may lead to systematic errors. Extensive efforts have been made to overcome these drawbacks, for example by matrix separation, thin-film formation, and mathematical corrections. Nevertheless, the new techniques of optical atomic spectrometry have surpassed conventional XRF in many respects.

From the start in 1895, X-rays were immediately applied to medical and dental diagnosis and later on for security checks at airports, for material analysis, ore mining, and pollution control. Furthermore, X-rays in astronomy have enlarged our view of the universe. In 1932, the “German Röntgen Museum” was founded at Röntgen’s birthplace in Lennep, 50 km away from Dortmund, Germany. Today it is a global center of the life, research, and impact of Wilhelm Conrad Röntgen and presents numerous valuable original objects of the discovery, development, and application of X-rays [9].

1.2 THE NEW VARIANT TXRF

Simultaneously with the invention of semiconductor devices in the “silicon valley” after 1970, a new kind of an X-ray detector was developed. It could not only count the individual X-ray photons but could also determine their energy. Such a Si(Li) detector was called “energy-dispersive” instead of the “wavelength-dispersive” spectrometers used so far. The novel detectors were small and compact, did not need a goniometer with an analyzing crystal, and could collect the whole spectrum simultaneously in a very short time.

1.2.1 Retrospect on its Development

Additional important progress in XRF was made 50 years after the discovery of total reflection of X-rays by Compton. In 1971, Yoneda and Horiuchi [10] evolved an ingenious idea of using total reflection for the excitation of X-ray fluorescence. They proposed the analysis of a small amount of material applied on a flat, even, and totally reflecting support. An energy-dispersive Si(Li) detector, developed shortly before, was placed directly above the support for

sample analysis. First, they determined uranium in sea water, iron in blood, and rare earth elements in hot-spring water. The theoretical basis and the experimental conditions were subsequently investigated. In Vienna, Austria, Wobrauschek wrote a PhD thesis on the subject [11], and together with Aiginger, they reported detection limits of nanograms [12,13]. In Geesthacht near Hamburg, Germany, Knoth and Schwenke found element traces on the ppb-level [14,15].

In the decade after 1980, a great variety of applications promoted a growing interest, and different instruments became commercially available (the “Wobi” module of the IAEA in Vienna, Austria; EXTRA II of Seifert in Ahrensburg, Germany; Model 3726 of Rigaku, Japan; TREX 600 of Technos, Japan; and TXRF 8010 of Atomika, Munich, Germany). The number of instruments in use increased to about 200 worldwide and the new variant of XRF turned out to have considerable advantages for spectrochemical analysis of different materials. At a first “workshop” in Geesthacht in 1986, the participants decided to call the new method “total reflection X-ray fluorescence analysis” and introduced the acronym “TXRF.” A series of biannual international meetings followed. Table 1.2 lists the years, locations, and chairpersons. The papers presented were subsequently published as proceedings in special issues of scientific journals, mostly of *Spectrochimica Acta* [16–27]. The next conference will be held in 2015 as a satellite meeting of the Denver conference in Denver, Colorado.

In 1983, an angular dependence of the fluorescence intensities in the range below the critical angle of total reflection was first observed by Becker *et al.* [28]. It led to the nondestructive investigation of surface contamination and thin near-surface layers. This variant was also called “grazing-incidence” XRF. In 1986, the X-radiation of a synchrotron was first used for excitation by Iida *et al.* [29]. The high intensity, linear polarization, and natural collimation of this X-ray source were shown to be very useful and favorable in comparison to conventional X-ray sources.

In 1991, Wobrauschek, Aiginger, Schwenke, and Knoth (Figure 1.5) won the distinguished Bunsen–Kirchhoff Prize of the DASp (Deutscher Arbeitskreis für Angewandte Spektroskopie) for the development of TXRF. In the years after, first reviews and book contributions were published on the subject of TXRF (e.g. [30,31]). They enclose short surveys with some 10 to 50 pages. In 1997, this monograph at hand was published in a first edition, exclusively dedicated to TXRF. It was very well received on the market and within one year after publication, 450 copies of the book were sold. Today, it is still the only comprehensive monograph on the field of TXRF. Nearly 800 copies of the first edition have been distributed and nearly 350 different scientific articles have used the book as a reference, so it is the most cited item in this field of research. In 2002, the English edition was translated into Chinese and offered as a low-price book.

The development of TXRF and related methods can be read from the rate of peer-reviewed papers. Figure 1.6 demonstrates the publication rate of XRF

TABLE 1.2. Fifteen TXRF-Meetings Between 1986 and 2013

No	Date	Type	Location	Country	Chairperson	Proceedings
1	May, 1986	Workshop	Geesthacht	Germany	Michaelis	GKSS Report 86/E/61 (1986)
2	May, 1988	Workshop	Dortmund	Germany	Klockenkämper	Spectrochim. Acta 44B (1989)
3	May, 1990	Workshop	Vienna	Austria	Aiginger, Wobrauschek	Spectrochim. Acta 46B (1991)
4	May, 1992	Workshop	Geesthacht	Germany	Andreas Prange	Spectrochim. Acta 48B (1993)
5	Sept, 1994	Workshop	Tsukuba/Tokyo	Japan	Yohichi Gohshi	Adv. X-ray Chem. Anal. Jpn. 26s (1995)
6	June, 1996	Conference	Eindhoven	Netherlands	de Boer	Spectrochim. Acta 52B (1997)
7	Sept, 1998	Conference	Dortmund	Germany	Klockenkämper	
8	Sept, 1998	Conference	Austin/Texas	USA	Mary Ann Zaitz	Spectrochim. Acta 54B (1999)
9	Sept, 2000	Conference	Vienna	Austria	Wobrauschek, Stireli	Spectrochim. Acta 56B (2001)
10	Sept, 2002	Symposium	Funchal/Madeira	Portugal	Maria Luisa de Carvalho	Spectrochim. Acta 58B (2003)
11	Sept, 2003	Conference	Awaji-Island	Japan	Yohichi Gohshi	Spectrochim. Acta 59B (2004)
12	Sept, 2005	Conference	Budapest	Hungary	Gyula Zaray	Spectrochim. Acta 61B (2006)
13	June, 2007	Conference	Trento	Italy	Giancarlo Pepponi	Spectrochim. Acta 63B (2008)
14	June, 2009	Conference	Gothenburg	Sweden	Johan Boman	Spectrochim. Acta 65B (2010)
14	June, 2011	Conference	Dortmund	Germany	Alex von Bohlen	
23	Sept, 2013	Conference	Osaka	Japan	Kouichi Tsuji	Virtual issue Spectrochim. Acta (2014)



Figure 1.5. Four pioneers of TXRF analysis, from left to right: Peter Wobrauschek, Hannes Aiginger, Heinrich Schwenke, and Joachim Knoth were awarded the “Bunsen–Kirchhoff Prize” in 1991. Photo by R. Klockenkämper, private property.

(Figure 1.6a) and TXRF (Figure 1.6b) within the last 40 years. The number of all XRF papers started in 1970 at a level of about 100 papers per year, remained constant for 20 years, and exponentially increased after 1990 to a rate of 2500 papers per year. Between 1970 and 1985, TXRF papers appeared only sporadically. But in the years after 1986, their number grew explosively from some 3 to about 125 papers per year with large fluctuations. The impact of the special issues after every single TXRF conference can be recognized as special peaks, repeating every 2 years after 1989. Altogether, 1250 articles have been published in the field of TXRF. It is interesting to mention that only eight authors are connected with 30% of all published papers in this field.

The method of TXRF has been developed significantly and has become a high-performance variant of classical X-ray fluorescence. For a lot of elements, the detection limits are on the pg-level and even below. In general, all elements except for the light elements can be detected. TXRF analysis can be compared with ET-AAS, which is the high-power specialty of FAAS, and with ICP-MS, which even tops ICP-OES. TXRF ranks high among these competitive methods of element spectral analysis.

In the last 15 years after the first edition of this monograph, different review articles on TXRF have been published summarizing new developments and results [32–34]. Book contributions furthermore describe the subject with different aspects, for example, wafer analysis [35–37]. Specific articles deal with further developments, such as excitation with synchrotron radiation [38,39], with standing waves by grazing incidence [40,41], with biological applications [42], with sample preparation [43], and with portable instruments [44]. Today, TXRF is successfully applied all over the world

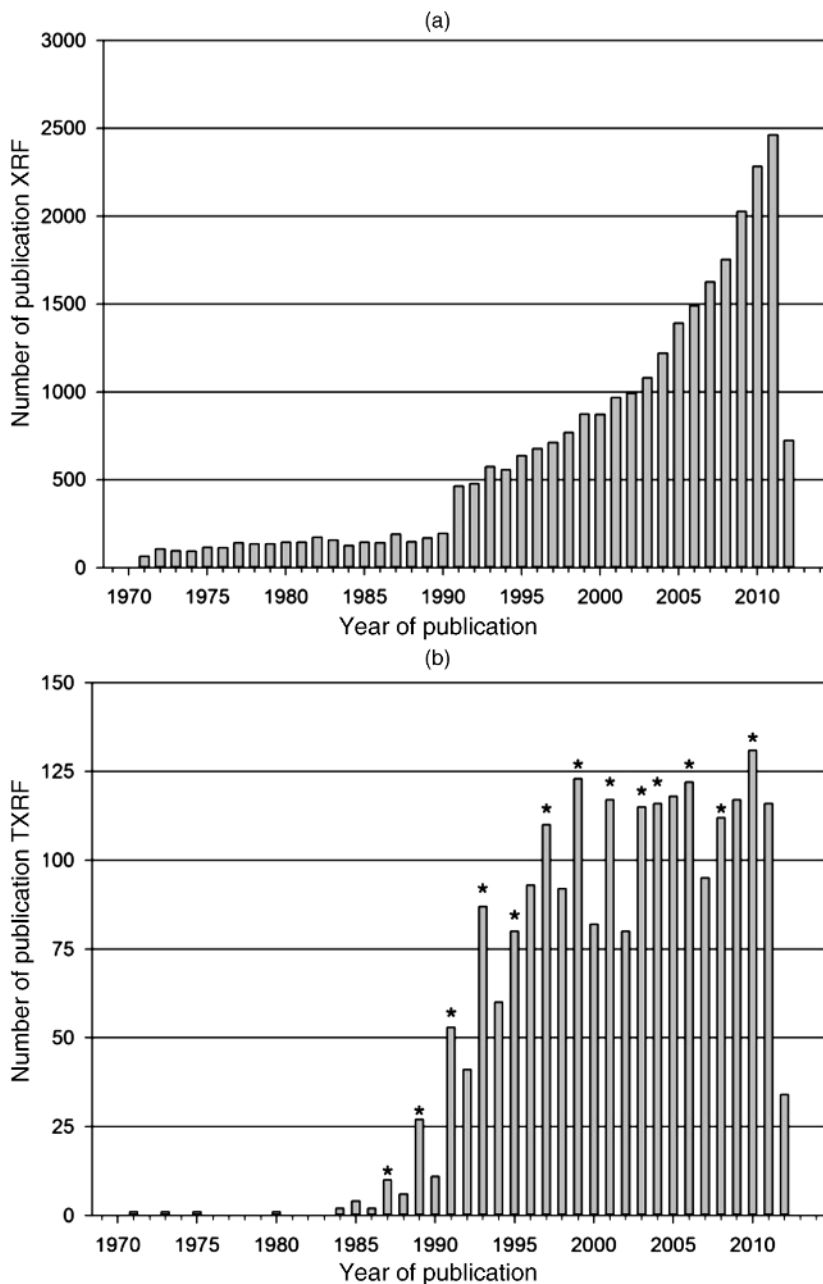


Figure 1.6. Number of annually published papers between 1970 and 2012 presented as bar plots. (a) For XRF in total. (b) Solely for TXRF. The data came from ISI Web of Knowledge, January 2012; <http://thomsonreuters.com>.

(see Section 6.3.3), and suitable equipment are installed and operated at several institutes and laboratories in a lot of countries: Argentina, Australia, Austria, Belgium, Brazil, Chile, China, Cuba, France, Germany, Great Britain, Hungary, India, Italy, Japan, Poland, Portugal, Russia, Spain, Sri Lanka, Sweden, Switzerland, Taiwan, The Netherlands, different states of the USA (CA, TX, IL, NM, ID, NY, MA, NJ, MD), Venezuela, and Vietnam. The users come from university institutes of chemistry and physics, from synchrotron beamlines at synchrotron facilities, and from chemical laboratories in industry, especially in the semiconductor industry—with particular interest in wafer production and control.

1.2.2 Relationship of XRF and TXRF

As is illustrated in Figure 1.7, TXRF is a variation of energy-dispersive XRF with one significant difference. In contrast to XRF, where the primary beam strikes the sample at an angle of about 40° , TXRF uses a glancing angle of less than 0.1° . Owing to this grazing incidence, the primary beam shaped like a strip of paper is totally reflected at the sample support.

Today, TXRF is primarily used for chemical *micro-* and *trace* analyses. For this purpose, small quantities, mostly of solutions or suspensions, are placed on optical flats (e.g., quartz glass) serving as sample support. After evaporation, the residue is excited to fluorescence under the fixed small glancing angle and the characteristic radiation is recorded by a Si(Li), or recently by a Si-drift detector, as an energy-dispersive spectrum. It is the *high reflectivity* of the sample support that nearly eliminates the spectral background of the support and lowers the detection limits from 10^{-7} to 10^{-12} g. Although this mode of operation does not permit the entirely nondestructive investigation of bulk material, it offers new challenging possibilities in ultramicro- and ultratrace analyses. Besides its high detection power, simplified quantification is made possible by internal standardization. This is because matrix effects cannot build up within the minute residues or thin layers of a sample.

A new field of application has been opened in the 1980s by *surface* and *near-surface layer* analyses. In 1983, the angular dependence of X-ray fluorescence at grazing incidence was investigated as already mentioned earlier [28]. This effect was used in the following years to investigate surface impurities, thin near-surface layers, and even molecules adsorbed on flat surfaces. Such examinations are especially applicable for cleaned and/or layered wafers representing the basic material for the semiconductor industry. The flat samples are examined either with respect to contamination of the surface or with respect to the setup of near-surface layers. However, this mode of analysis needs fluorescence intensities to be recorded not only at one fixed angle but at various angles around the critical angle of total reflection. From these angle-dependent intensity profiles, the composition, thickness, and even density of top layers can be ascertained. It is the *low penetration depth* of the primary beam at total reflection that enables this in-depth examination of ultrathin

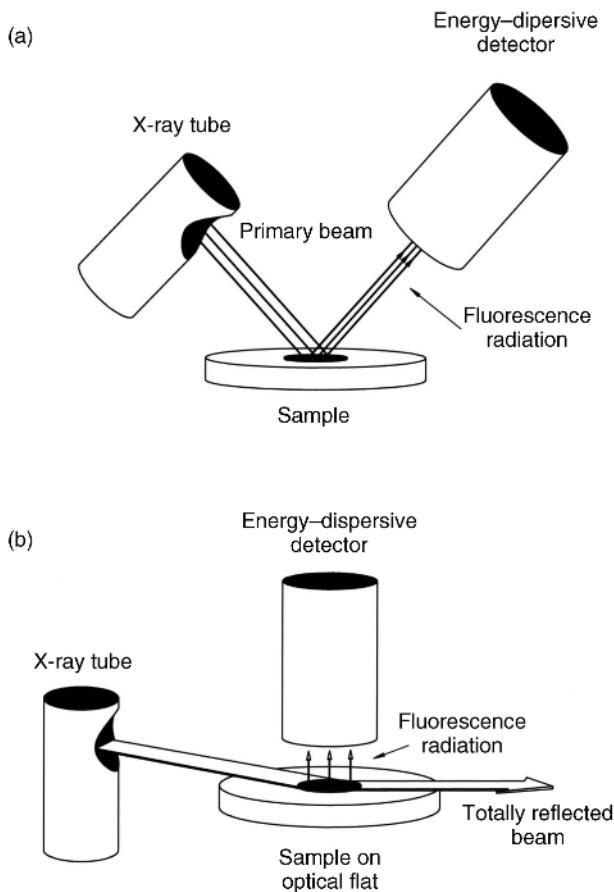


Figure 1.7. Instrumental arrangement for (a) conventional XRF and (b) TXRF. Comparison shows a difference in the geometric grouping of excitation and detection units. Figure from Ref. [8], reproduced with permission. Copyright © 1996, John Wiley and Sons.

layers in the range of 1–500 nm. The method is nondestructive and needs no vacuum—at least no ultrahigh vacuum (UHV).

In spite of the similarities in instrumentation, such as the X-ray source, the energy-dispersive detector, and pulse-processing electronics, the use of TXRF differs fundamentally from classical XRF. With respect to sample preparation and performance of analysis, it has a lot in common with AAS or ICP for trace element analysis and it is similar to X-ray photoelectron spectroscopy (XPS), Rutherford backscattering spectroscopy (RBS), and secondary ion mass spectrometry (SIMS) for surface and near-surface layer analysis. In fact, TXRF is able to compete, often favorably, with these well-established methods.

The main reason for this progress is the special geometric arrangement leading to total reflection of the primary beam. Accordingly, the totally reflected beam interferes with the incident primary beam and leads to standing waves above surfaces and also within near-surface layers. The unique role of TXRF is based on the formation of such standing waves and particular details can only be understood with regard to these standing waves.

The arrangement of grazing incidence is not restricted to XRF measurements. It can also be exploited for X-ray reflection (XRR) and X-ray diffraction (XRD). As early as 1931, Kiessig investigated the reflection of thin layers deposited on a thick substrate [45], and in 1940, Du Mond and Youtz observed Bragg-reflection of periodic multilayers [46]. It was not until the late 1970s that XRD at grazing incidence was developed. This monograph mainly deals with the technique of TXRF and excludes that of XRD. However, reports of XRR experiments are included when needed for a better understanding or even for complementary results. The usual TXRF instrumentation can simply be extended for such experiments.

1.3 NATURE AND PRODUCTION OF X-RAYS

Already in the seventeenth century, Isaac Newton described visible light as a beam of small corpuscles while Christian Huygens developed a picture of a beam with waves. In the corpuscle picture, all corpuscles travel at the velocity of light c . They follow straight lines that can be regarded as beams. In the wave picture, the light propagates as a wave showing crests and troughs. They follow each other with a frequency ν and at a distance λ called the wavelength and are always orthogonal to the direction of the respective beam. The speed of light in vacuum was shown to be nearly 3×10^8 m/s. Phenomena of reflection, refraction, diffraction, and polarization could be explained in the one or in the other picture, or even in both pictures. The wavelength of visible light was determined to lie between 0.4 and 0.8 μm .

In 1865, James Clerk Maxwell described light as an *electromagnetic* wave with electric and magnetic field strength. The photoelectric effect as a reaction of radiation with matter was explained by Einstein in 1905. Together with Planck he identified a light beam as an array of energy quanta called photons. A photon was defined as a corpuscle that carries an elementary energy unit E but has no rest mass. *In vacuo*, all photons travel at the velocity of visible light on straight lines. However, the dualism of the corpuscular and the wave picture was not dissolvable; neither corpuscles nor waves could have been seen directly, only the different phenomena have been observed.

1.3.1 The Nature of X-Rays

Shortly after their discovery by Röntgen in 1895, X-rays were assumed to be part of the electromagnetic radiation. Von Laue and the Braggs explained the

diffraction of X-rays in the wave picture and measured wavelengths of about 0.1 nm. Such values are comparable with the spacing of crystal lattice planes. This value d was previously determined for simple crystals from Avogadro's number, the molecular mass, and the density, for example, for a rock salt crystal [1].

In order to describe the incoherent scattering of X-rays by electrons, Arthur H. Compton used the corpuscle picture. On the other side, in 1923 he detected the external total reflection of X-rays that again supported the hypothesis of the wave nature of X-rays. This dualism of a corpuscular and a wave picture was interpreted as a complementary nature of the electromagnetic radiation. It was overcome in 1927 by Niels Bohr in Copenhagen. Because of Heisenberg's uncertainty principle, the location of corpuscles cannot be determined with absolute certainty. The locus can be estimated by quantum mechanics only as a statement of probability expressed by a wave function.

X-ray photons have energies in the kilo-electronvolt range (0.01–100 keV) and wavelengths in the nanometer range (100–0.01 nm). Figure 1.8 demonstrates X-rays as a part of the wide electromagnetic spectrum including synchrotron radiation. Photon energy and wavelength are inversely proportional, according to

$$E = h\nu = \frac{hc}{\lambda} \quad (1.1)$$

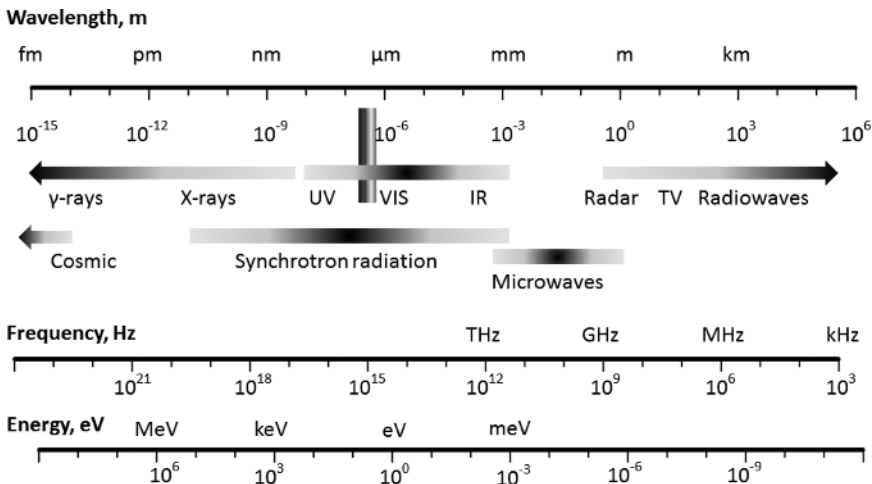


Figure 1.8. Spectrum of the electromagnetic radiation with wavelengths between 1 fm and 1000 km covering more than 21 orders of magnitude. The visible light appears in the very small region between 390 and 770 nm (gray ribbon VIS). X-rays span about four orders of magnitude far below the visible and the ultraviolet light (UV). The radiation of synchrotrons has a width of eight orders of magnitude.

where h is the Planck's constant and c is the speed of light ($h \approx 4.136 \times 10^{-15}$ eV·s; $c \approx 2.998 \times 10^8$ m/s).

The conversion of energy and wavelength of Equation 1.1 can be made by the simple relationship

$$E[\text{keV}] \approx \frac{1.23984}{\lambda[\text{nm}]} \quad (1.2)$$

Frequently used physical constants are listed in Table 1.3 with the latest numerical values from NIST (National Institute of Standards and Technology, Gaithersburg, MD). They are given in SI units, mostly with 9 to 11 digits and with a relative uncertainty of some 10^{-8} [47]. The values with SI units can be transformed into atomic units by the relationship $1 \text{ J} = 6.241 509 34 \times 10^{18} \text{ eV}$. In the text, physical constants will be given with only 3 to 5 digits and atomic units.

1.3.2 X-Ray Tubes as X-Ray Sources

X-rays are originally produced by the bombardment of matter with accelerated electrons. Usually, such a *primary* radiation is produced by an X-ray tube of the Coolidge-type as mentioned earlier and shown in Figure 1.4. It consists of a vacuum-sealed tube with a metal-glass cylinder. A tungsten filament serves as hot cathode, and a pure-metal target, such as chromium, copper, molybdenum, or tungsten, serves as the anode. Electrons are emitted from the heated filament and accelerated by an applied high voltage in the direction of the anode. The high-energy bombardment of the target produces heat above all while the electrons are absorbed, retarded, or scattered. Finally, X-rays and Auger electrons can be produced. The heat is dissipated by water-cooling of the anode while the X-rays emerge from a thin exit window as an intense X-ray beam. Mostly, a 0.2–1 mm thick beryllium window is used. Reflected electrons, including Auger electrons, cannot escape from this window.

The X-ray tube is supplied by a stabilized high-voltage generator. High voltage and current applied to the tube determine the intensity of the X-ray beam. The voltage can usually be chosen between 10 and 60 or even 100 kV, the current between 10 and 50 mA, so that an electric power of several kilowatts can be supplied. However, only about 0.1% of the electric input power is converted into radiation and most of it is dissipated as heat. For that reason, such X-ray tubes have to be cooled intensively by water. A flow rate of 3 to 5 l/min is commonly needed.

The primary X-ray beam is normally used to irradiate a sample for analysis. By this *primary* irradiation, the atoms in the sample are generally excited to produce *secondary* X-rays by themselves. This effect is called X-ray fluorescence. The secondary radiation can be used as a color pattern of the sample as its *chromatic* composition changes with the *element* composition. The spectral pattern can be recorded like a barcode by means of an X-ray detector and constitutes the basis of XRF analysis.

TABLE 1.3. Some Frequently Used Physical Constants from NIST Reference Values [47]

Term of the Constant	Character	Numerical Value	Uncertainty	SI Unit	Relative Unc.
Avogadro's constant	N_A	$6.022\,141\,29 \times 10^{23}$	$0.000\,000\,27 \times 10^{23}$	mol^{-1}	4.1×10^{-8}
Boltzmann's constant	k	$1.380\,648\,8 \times 10^{-23}$	$0.000\,001\,3 \times 10^{-23}$	J/K	9.1×10^{-7}
Compton wavelength	λ_C	$2.426\,310\,238\,9 \times 10^{-12}$	$0.000\,000\,001\,6 \times 10^{-12}$	m	6.5×10^{-10}
Electric constant	ϵ_0	$8.854\,187\,817 \times 10^{-12}$	exact	As/Vm	
Electron radius, classical	r_e	$2.817\,940\,326\,7 \times 10^{-15}$	$0.000\,000\,002\,7 \times 10^{-15}$	m	9.7×10^{-10}
Electron rest energy	E_0	$8.187\,105\,06 \times 10^{-14}$	$0.000\,000\,36 \times 10^{-14}$	eV	4.4×10^{-8}
Electron rest mass	m_0	$9.109\,382\,91 \times 10^{-31}$	$0.000\,000\,40 \times 10^{-31}$	kg	4.4×10^{-8}
Elementary charge	e	$1.602\,176\,565 \times 10^{-19}$	$0.000\,000\,035 \times 10^{-19}$	C = As	2.2×10^{-8}
Fine structure constant	α_f	$7.297\,352\,569\,8 \times 10^{-3}$	$0.000\,000\,002\,4 \times 10^{-3}$	dimensionless	3.2×10^{-10}
Inverse fine structure constant	$1/\alpha_f$	137.035 999 074	0.000 000 044	dimensionless	3.2×10^{-10}
Magnetic constant	μ_0	$12.566\,370\,614 \times 10^{-7}$	exact = $4\pi \times 10^{-7}$	N/A ²	
Planck's constant	h	$6.626\,069\,57 \times 10^{-34}$	$0.000\,000\,29 \times 10^{-34}$	Js	4.4×10^{-8}
Planck's constant over 2π	\hbar	$1.054\,571\,726 \times 10^{-34}$	$0.000\,000\,047 \times 10^{-34}$	Js	4.4×10^{-8}
Proton rest mass	m_p	$1.672\,621\,777 \times 10^{-27}$	$0.000\,000\,074 \times 10^{-27}$	kg	4.4×10^{-8}
Proton-electron mass ratio	m_p/m_0	1836.152 672 45	0.000 000 75	dimensionless	4.1×10^{-10}
Rydberg's constant	R_∞	$10.973\,731\,568\,539 \times 10^6$	0.000 055	m^{-1}	5.0×10^{-12}
Speed of light <i>in vacuo</i>	c_0	$2.997\,924\,58 \times 10^8$	exact = $1/\sqrt{\epsilon_0\mu_0}$	m/s	

Contribution of the National Institute of Standards and Technology.

X-ray spectra generally show the intensity of radiation or rather the number of its photons in relation to the wavelength of radiation or the energy of these photons. Normally, X-ray spectra consist of two different parts, the line spectrum and the continuous spectrum.

1.3.2.1 The Line Spectrum

A line spectrum will be produced if a target or sample is irradiated with X-ray photons, as just mentioned, or is bombarded with electrons (or ions). In both cases a sufficient energy of photons or electrons is needed. The energy must exceed the binding energy of a bound inner electron of the target atoms, which therefore is called the *critical excitation energy*. The ensuing effects can be described best by Niels Bohr's atomic model, which supposes Z electrons revolving around a nucleus in different orbitals or shells and subshells, where Z is the atomic number of the respective element.

Owing to the high-energy impact, an inner electron can be ejected from the atom so that a vacancy is created within the respective inner electron shell. The atom with the vacancy is in an instable state of higher energy and tries to regain its stable ground state by two different processes. In both processes an outer bound electron fills the vacancy and the atom instantly emits either an X-ray photon, which is the basic process of XRF, or what is called an Auger electron. The energy of the X-ray photon must be equal to the difference of the previous and the subsequent energy state of the atom:

$$E_{\text{photon}} = E_{\text{previous}} - E_{\text{subsequent}} \quad (1.3)$$

The newly created vacancy in the outer shell can be filled in turn by an electron still farther out, and another X-ray photon can be emitted. These processes will follow each other successively and a series of photons will be emitted until a free electron ultimately replaces an outermost valance electron so that the atom has finally returned to the ground state.

Since the energy states of atomic electrons are quantized and characteristic of all atoms of an element, the X-ray photons emitted in this way have individual energies that are equal for all atoms of the same element but different for atoms of different elements. Consequently, these photons cause discrete sharp lines or peaks as intensity maxima in an X-ray spectrum that are characteristic for any single element of the sample target. Conversely, any element of the sample can be identified by its characteristic lines or peaks, comparable to a fingerprint or barcode. For this reason, the line spectra are also called *characteristic spectra*. Of course, line spectra of the same sample either produced by X-ray photons or by electrons are similar.

Although not every outer electron is permitted to fill an inner vacancy, there are a lot of allowed transitions according to the selection rules of quantum theory. The most important transitions are indicated in Figure 1.9

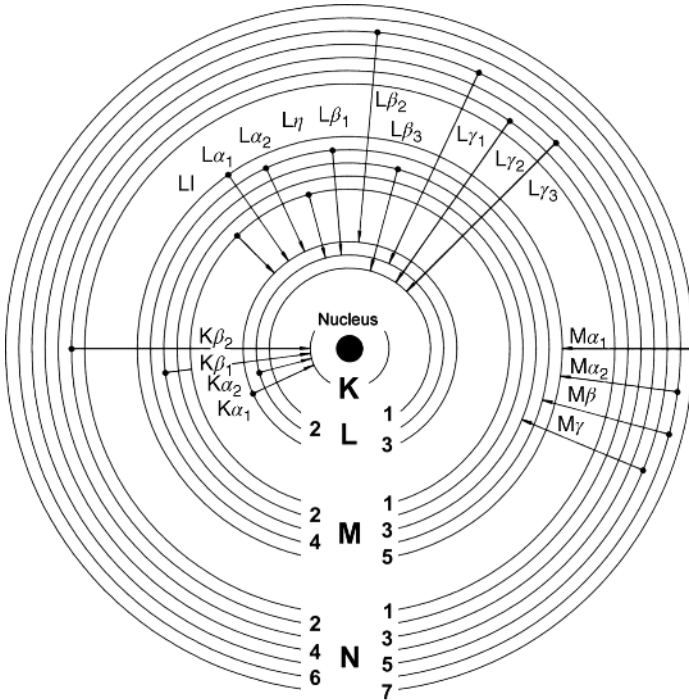


Figure 1.9. Electron transitions that are possible in a heavy atom and that produce the principal lines or peaks within an X-ray spectrum. Figure from Ref. [8], reproduced with permission. Copyright © 1996, John Wiley and Sons.

(see, e.g., Ref. [48]). They lead to the principal lines or peaks named here in the classical notation. There are three principal series, the K, L, or M series, which arise when the inner vacancy being filled is in the K, L, or M shell. A series contains several peaks named K, L, or M peaks, which mainly differ according to the origin of the outer electron. The most intense peak is called α , the next less intense peaks in descending order are called β , γ , η , and ι . A further differentiation is made by an Arabic numeral added as an index, such as α_1 and α_2 for the α doublet. This classical notation proposed by Siegbahn after 1920 is not entirely systematic and indeed somewhat confusing. Meanwhile, the International Union of Pure and Applied Chemistry (IUPAC) has suggested a nomenclature that is solely based on the shell and subshell designation. Table 1.4 compares the K and L peaks in both notations [49].

From the preceding discussion it can be understood that the two lightest elements hydrogen and helium have no X-ray peaks at all because of their lack of inner electrons. However, all other elements have characteristic X-ray peaks. They appear in a spectrum with an intensity that depends on the energy of the primary X-rays or electrons, on the composition of the sample target, and on the efficiency of the detector. In the range up to 40 keV, normally each

TABLE 1.4. K and L X-ray Lines or Peaks in Siegbahn and IUPAC Notation

Siegbahn	IUPAC	Siegbahn	IUPAC	Siegbahn	IUPAC	Siegbahn	IUPAC
$K\alpha_1$	K-L ₃	L α_1	L ₃ -M ₅	L γ_1	L ₂ -N ₄	M α_1	M ₅ -N ₇
$K\alpha_2$	K-L ₂	L α_2	L ₃ -M ₄	L γ_2	L ₁ -N ₂	M α_2	M ₅ -N ₆
$K\beta_1$	K-M ₃	L β_1	L ₂ -M ₄	L γ_3	L ₁ -N ₃	M β	M ₄ -N ₆
$K\beta_2^I$	K-N ₃	L β_2	L ₃ -N ₅	L γ_4	L ₁ -O ₃	M γ	M ₃ -N ₅
$K\beta_2^{II}$	K-N ₂	L β_3	L ₁ -M ₃	L γ'_4	L ₁ -O ₂	M ζ	M _{4,5} -N _{2,3}
$K\beta_3$	K-M ₂	L β_4	L ₁ -M ₂	L γ_5	L ₂ -N ₁		
$K\beta_4^I$	K-N ₅	L β_5	L ₃ -O _{4,5}	L γ_6	L ₂ -O ₄		
$K\beta_4^{II}$	K-N ₄	L β_6	L ₃ -N ₁	L γ_8	L ₂ -O ₁		
$K\beta_{4x}$	K-N ₄	L β_7	L ₃ -O ₁	L γ'_8	L ₂ -N _{6,7}		
$K\beta_5^I$	K-M ₅	L β_8	L ₃ -N _{6,7}	L η	L ₂ -M ₁		
$K\beta_5^{II}$	K-M ₄	L β_9	L ₁ -M ₅	L ι	L ₃ -M ₁		
		L β_{10}	L ₁ -M ₄	L σ	L ₃ -M ₃		
		L β_{15}	L ₃ -N ₄	L τ	L ₃ -M ₂		
		L β_{17}	L ₂ -M ₃	L υ	L ₃ -N _{6,7}		
				L ν	L ₂ -N _{6,7}		

Source: From Ref. [49], reproduced with permission. Copyright © 1996, John Wiley and Sons.

element apart from H and He shows between 2 and about 10 intensive peaks, so that X-ray spectra in contrast to ultraviolet (UV) spectra can be regarded as fortunately poor in peak number. Figure 1.10 shows some examples for different pure elements excited at 40 keV. The lighter elements up to $Z=25$ mostly show a $K\alpha$ doublet, which is not resolved here, and a $K\beta$ peak at higher energy. The heavier elements with $25 < Z < 57$ additionally have several L peaks mostly with an α doublet followed by a more energetic β and γ group. Heavy elements with $Z > 57$ are lacking in K peaks (their exciting potential is >40 keV) but show some M peaks in addition to the L peaks. In general, the most intensive K or L peaks are used for X-ray spectral analysis.

As mentioned earlier, the relationship of peak or photon energy and element was discovered by Moseley in 1913. He found that the reciprocal wavelength and consequently the photon energy are dependent on the atomic number Z of the elements. His well-known law can be described by

$$E_{ij} = k_{ij} \cdot (Z - \sigma_i)^2 \quad (1.4)$$

with certain constant values k_{ij} and σ_i for particular peaks or lines, j , of a series, i . This square law is demonstrated in Figure 1.11 by different parabolas, each representing a particular peak (see, e.g., Bertin [48]). As a consequence of Moseley's law, the atomic number of the elements could be ascertained beyond any doubt.

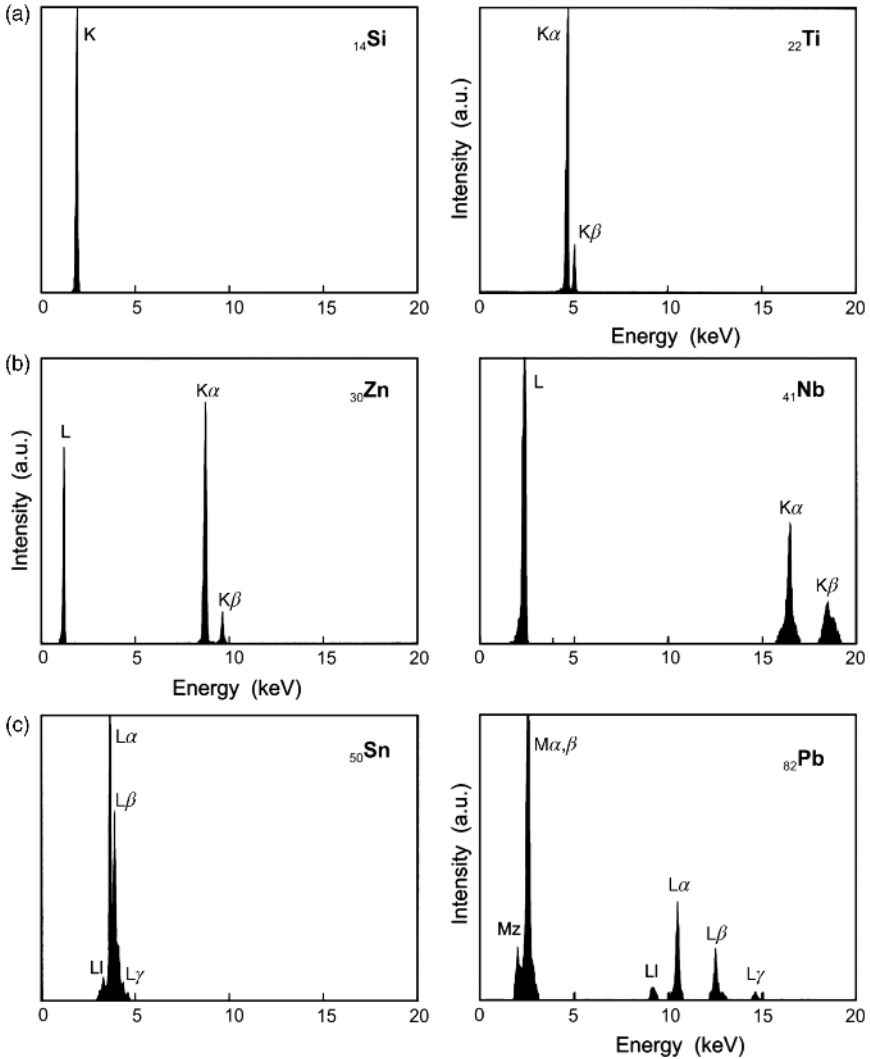


Figure 1.10. X-ray spectra with K lines of silicon and titanium (a), with L and K lines of zinc and niobium (b), and with L and M lines of tin and lead (c). The fluorescence intensity in arbitrary units is plotted against the photon energy in keV. Figure from Ref. [8], reproduced with permission. Copyright © 1996, John Wiley and Sons.

Quantum mechanics of atoms that are missing one single electron in an inner shell can explain Moseley's law. The values k_{ij} can be derived from

$$k_{ij} = R_E \cdot \left(\frac{1}{n_i^2} - \frac{1}{n_j^2} \right) \quad (1.5)$$

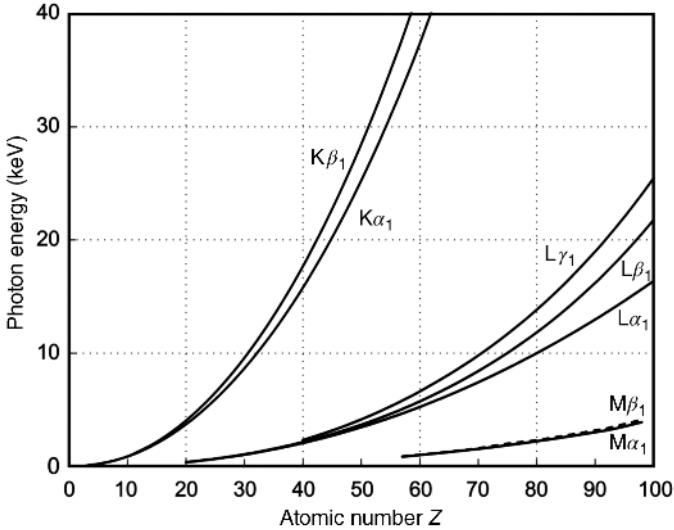


Figure 1.11. Moseley diagram of photon energies of the principal X-ray emission peaks dependent on the atomic number Z of the elements. Figure from Ref. [8], reproduced with permission. Copyright © 1996, John Wiley and Sons.

where R_E is bound up with the Rydberg energy, $R_\infty = R_E/hc$, which amounts to 13.606 eV (the binding energy of the 1s electron of hydrogen), and n_i and n_j are the principal quantum numbers of the involved inner and outer electrons, respectively, of the atom emitting the X-ray photon.

The quantities k_{ij} and σ_i characterize the different peaks. The factor k_{ij} for $K\alpha_1$ peaks is 10.20 eV, for the $L\alpha_1$ peaks is 1.89 eV, and for the $M\alpha_1$ peaks is 0.66 eV. The quantity σ_i can be interpreted as a shielding constant. From the point of view of an outer electron, it may be defined as that number of negative electrons by which the number of positive charges of the nucleus is reduced. $(Z - \sigma_i)$ may be defined as the effective nuclear charge. The σ_i values are not exactly equal for all elements but somewhat dependent on their atomic number Z . As listed in Table 1.5, experimental values for $K\alpha_1$ peaks are below 1.0; for $K\beta_1$ peaks, below 1.9; for $L\alpha_1$ peaks, below 7.4; and for $M\alpha_1$ peaks, at about 22.

The minimum excitation potential for the appropriate spectral series i can also be determined after Moseley's law. An inner electron of a target atom can only be expelled from its shell by an accelerated electron in the X-ray tube if its energy is above a minimum energy, E_{\min} , also called critical excitation energy. During this process, the quantum number n_i of the inner electron changes to $n_j = \infty$, leading to

$$E_{\min} = R_E(Z - \sigma_i)^2 \left(\frac{1}{n_i}\right)^2 \tag{1.6}$$

TABLE 1.5. Factors k_{ij} and Shielding Constants σ_i of Characteristic X-Ray Lines and Absorption Edges Experimentally Determined for Several Elements According to Moseley's Law

Quantum Number	$K\alpha_1$	$K\beta_1$	K Edge	$L\alpha_1$	L_3 Edge	$M\alpha_1$	M_4 Edge
n_j , initial	2	3	1	3	2	4	3
n_i , final	1	1	∞	2	∞	3	∞
k_{ij} [eV]	10.204	12.094	13.606	1.890	3.401	0.661	1.512

Atomic Number Z	σ_i for $K\alpha_1$	σ_i for $K\beta_1$	σ_i for K Edge	σ_i for $L\alpha_1$	σ_i for L_3 Edge	σ_i for $M\alpha_1$	σ_i for M_4 Edge
6–10	0.83						
11–15	0.93	1.64	2.11				
16–20	0.97	1.73	2.52				
21–25	0.97	1.80	2.85				
26–30	0.93	1.87	3.14	6.73	12.14		
31–35	0.86	1.87	3.38	6.95	13.26		
36–40	0.74	1.84	3.56	7.08	14.17		
41–45	0.57	1.76	3.66	7.19	14.94		
46–50	0.34	1.61	3.69	7.28	15.67		
51–55		1.48	3.67	7.34	16.37	21.35	32.93
56–60				7.39	17.08	21.46	33.92
61–65				7.40	17.76	21.65	35.28
66–70				7.39	18.43	21.85	36.87
71–75				7.35	19.07	22.08	38.31
76–80				7.31	19.67	22.29	39.67
81–85				7.25	20.20	22.47	40.86
86–90				7.20	20.64	22.61	41.85
91–95						22.68	42.39

For the K series with $n_i=1$, σ_i takes experimental values of about 3; for the L series with $n_i=2$, σ_i values lie around 17; and for the M series with $n_i=3$, these values are around 39. E_{\min} is also the minimum energy of photons, needed for the excitation in X-ray fluorescence when a sample is irradiated by an X-ray tube. And it gives the position of the absorption edges of the different K-, L-, or M-shells (see Section 1.4.1). The respective characteristic peaks of the elements always lie just below these edges.

Moseley's law is not very stringent since relative deviations of 0.1–0.2% for the lines and of 0.5–2% for the edges occur. Consequently, the exact positions of characteristic X-ray lines and respective edges are not calculated in practice by using this law but instead are obtained from tables or computer memories with measured values. They normally give the energies and wavelengths of the peaks and additionally their relative intensities within the defined K, L, or M series. The relative intensity of a certain peak in its series is determined by the

probability of the electron transition causing this particular peak. The respective quantity is called emission rate g_{ij} and can be calculated from quantum mechanics. In general, the relative intensities are rather similar for most elements. For the K peaks, $K\alpha : K\beta$ is about 100:15; for the L peaks, $L\eta : L\alpha : L\eta : L\beta : L\gamma_1 : L\gamma_3$ is round 3:100:1:70:10:3; and for the M peaks, $M\alpha : M\beta : M\gamma$ is about 100:50:4.

The intensity of the total K, L, and M series is a function of the fluorescence yield ω_i . It gives the relative frequency according to which an X-ray photon and not an Auger electron is emitted after excitation of an atom. The relationship can be described approximately by

$$\omega_i = \frac{Z^4}{A + Z^4} \tag{1.7}$$

The constant A is about 9×10^5 for the K series; it is about 7×10^7 for the L series; and 1×10^9 for the M series.

The fluorescence yield for the K, L, and M series (see, e.g., Bertin [48]) correlates with the atomic number Z as shown in Figure 1.12. As demonstrated there, the X-ray photon and Auger electron emission are two competing effects, the frequencies of which sum up to 100%. The Auger process predominates for lighter elements, so that X-ray spectral analysis is not very effective for those elements with atomic numbers $Z < 20$ and especially for $Z < 10$. But for these elements, Auger spectroscopy is highly effective.

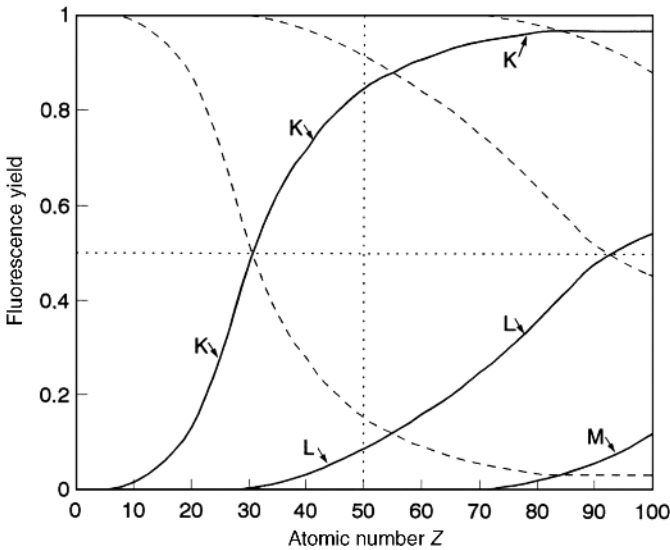


Figure 1.12. Fluorescence yield (—) and Auger electron yield (---) as a function of the atomic number Z of the emitter. Figure from Ref. [8], reproduced with permission. Copyright © 1996, John Wiley and Sons.

The intensity of any characteristic line of a target element can be expressed in number of photons emitted per unit time or second. For lines in the primary X-ray spectrum, for example, produced by electrons of an X-ray tube, this intensity can be given by an empirical formula:

$$N_{\text{line}}(E_{ij}) = kI g_{ij} \omega_i \cdot E_{\text{min}}^m (E_0/E_{\text{min}} - 1)^m \quad (1.8)$$

where $N_{\text{line}}(E_{ij})$ is the number of photons with E_{ij} , k is a constant, I is the electron current, g_{ij} is the emission rate of the respective line, i , in its series, j , ω_i is the fluorescence yield of the target material, E_0 is the accelerating potential of the X-ray tube, and E_{min} is the critical excitation energy for the appropriate spectral series. The exponent, m , usually has a value below 2. It may be $5/3$ for $E_{\text{min}} < E_0 < 2E_{\text{min}}$, and slowly decreases to 1.0 for E_0 values $> 5E_{\text{min}}$. This equation for target lines is rather simple compared to the formula for a secondary X-ray spectrum produced by X-ray fluorescence of a sample.

There are some exceptions to the aforementioned selection rules. First, there are emission peaks that do not correspond to permitted transitions and therefore are called “forbidden” peaks. Second, there are additional peaks that arise from a double ionization by a simultaneous impact of photons or electrons on two inner electrons of the atom. As the energy levels of the doubly ionized atom slightly differ from those of the singly ionized atom, somewhat different peaks occur, which are called “satellite” peaks. Forbidden and satellite peaks are always weak, and satellites mainly appear in the K-spectra of lighter elements. Nevertheless, they must not be ignored in trace analysis if they are generated by a major component at energies close to small peaks of trace elements. Consequently, both forbidden and satellite peaks are also included in tables or stored in computers.

According to their energy position, the characteristic X-ray peaks are independent of the chemical bonding or state of the atoms. This advantage exists as long as only electrons from inner shells are involved in the X-ray emission process and as long as these electrons are not affected by the chemical vicinity of the atoms. In practice, this is the normal situation for the detection of higher photon energies and heavier elements. However, exceptions can appear for lower energies and lighter elements. If an electron from a valence or a near valence band is involved in the emission process, the respective energy level of the atom and the energy transition will be affected by the chemical state. Consequently, the characteristic peaks may be shifted for elements in different compounds. As the effect is in the range of a few electronvolts, it can be measured and used to get information on chemical bonding. However, other spectroscopic techniques are more efficient in this respect. For the usual X-ray spectrometrical practice, peak shifts are an exception but may be taken into account to avoid systematic errors.

1.3.2.2 The Continuous Spectrum

This kind of spectrum is defined by an intensity distributed continuously over a broad range of energy or wavelength covering about three orders of magnitude. For this reason, it is called “continuous” or “white spectrum.” It is originally produced by energetic electrons or ions bombarding a target but actually not by X-ray photons themselves. However, if X-rays of a continuous spectrum are used to excite a sample, they will partly be scattered by this target and the original primary spectrum will be transformed into a somewhat modified spectrum that is likewise continuous but much smaller. Consequently, a continuous spectrum is present in any case, representing an inconvenient “background” that has to be eliminated from the analytical point of view. An example of a continuous spectrum produced by an X-ray tube is given in Figure 1.13. The characteristic L lines of the tube target are shown in addition.

A spectral continuum is produced by the fact that electrons penetrating into a target material are decelerated or retarded by impacts with the atomic nuclei of the target. The primary electrons lose their energy in these inelastic collisions, and this energy can be emitted as X-ray photons. A single electron can lose its energy completely in a single collision or stepwise in several consecutive collisions. Consequently, one single photon can be produced with the total electron energy or several photons with smaller parts of this energy. This is described in the corpuscular picture of X-ray photons with different energies.

In an X-ray tube operated at a voltage U_0 the electrons get the final energy E_0 according to

$$E_0 = e \cdot U_0 \quad (1.9)$$

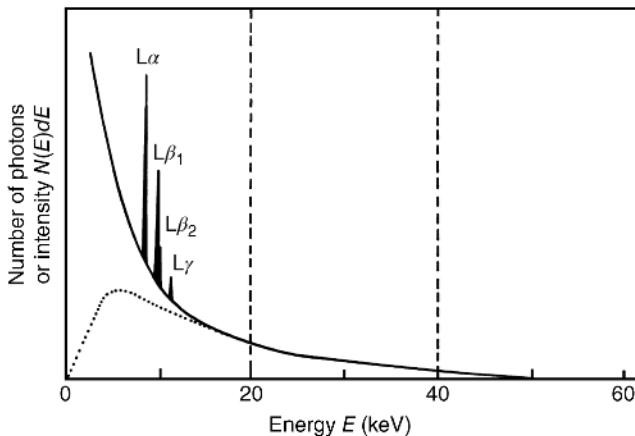


Figure 1.13. Spectrum of an X-ray tube operated at 50 kV and equipped with a thin target layer of tungsten as the anode. The spectrum is represented in the energy-dispersive mode. The K lines, with an excitation energy of 69.5 keV, cannot arise; but all L lines with a required minimum of 12.1 keV appear. The continuum of a thick solid target is illustrated by the dotted line. Figure from Ref. [8], reproduced with permission. Copyright © 1996, John Wiley and Sons.

where e is the charge of a single electron, called elementary charge ($e \approx 1.602 \times 10^{-19}$ Coulomb). Consequently, photons can carry away this maximum energy E_0 or lower energies down to zero. The spectrum covers the energy range between zero and the upper limit E_0 as shown in Figure 1.13. Since the retardation of electrons causes the continuous or white spectrum, this radiation is called *bremstrahlung* in German (*bremsen* = to brake and *Strahlung* = radiation). The intensity distribution of the *brem*-continuum can approximately be described by

$$N(E)\Delta E \approx kIZ \left(\frac{E_0}{E} - 1 \right) \Delta E \quad (1.10)$$

where $N(E)\Delta E$ is the number of photons emitted with energies between E and $E + \Delta E$, k is a constant, I is the tube current, and Z is the (mean) atomic number of the target. The formula shows the intensity or number of photons per second; it is inversely related to the energy of these photons, decreasing to zero when E approximates E_0 . The graph of Figure 1.13 does not touch the energy-axis but it cuts this axis under the angle $\arctan(-kIZE_0)$. Furthermore, Equation 1.10 indicates that the intensity can be increased linearly by the tube current, the applied voltage (by virtue of E_0), and by the atomic number of the target material. Simultaneously, the line intensity is increased and the detection limits are lowered (see Section 6.1.2). For that reason, high-powered X-ray tubes equipped with a heavy-metal anode are usually applied in X-ray fluorescence analysis.

Equation 1.10 can be transformed into a wavelength-dependent equation known as Kramers' formula:

$$N(\lambda)\Delta\lambda \approx kIZ \left(\frac{\lambda}{\lambda_0} - 1 \right) \frac{1}{\lambda^2} \Delta\lambda \quad (1.11)$$

where λ_0 corresponds to E_0 according to the Duane–Hunt law, $\lambda_0 = h \cdot c / E_0$. The relationship 1.11 is represented in Figure 1.14, which shows a sharp short-wavelength limit at λ_0 , a broad hump with a maximum at

$$\lambda_{\max} = 2 \lambda_0 \quad (1.12)$$

and an extended long-wavelength tail [50].

The effects of target irradiation by electrons are highly complex and not completely understood. Consequently, the two spectral distributions of the continuum given by Equations 1.10 and 1.11 are only valid for thin target layers where electron backscattering and other effects can be ignored. For thick solid targets, they are approximations that are reasonably well in the high-energy or short-wavelength region (hard X-rays). For low energies or long wavelengths (soft X-rays), however, they are substantially modified by the self-absorption of

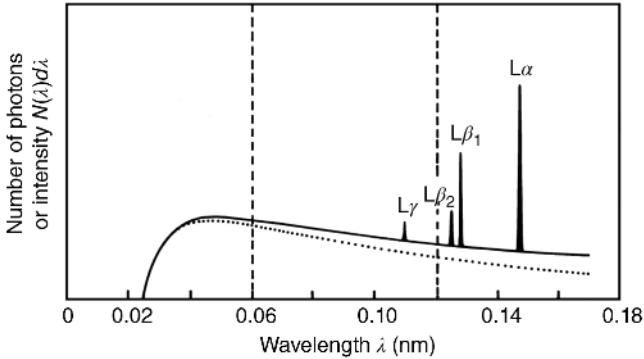


Figure 1.14. Spectrum of Figure 1.13 represented in the wavelength-dispersive mode. The X-ray tube operated at 50 kV may be equipped with a thin target layer (—) or a thick solid target (·····) (see also Ref. [50]). Figure from Ref. [8], reproduced with permission. Copyright © 1996, John Wiley and Sons.

X-rays within the target itself. These absorption losses reduce the continuous spectrum, and this effect is further increased by the absorption of X-rays in the exit window of the X-ray tube. In the end, a quite different dotted curve results for the soft X-ray region. Figure 1.13 shows the corresponding continuum of a thick target with a maximum at E_{\max} significantly below $0.5 \cdot E_0$ whereas the respective distribution for a thin layer has no relative maximum at all. Figure 1.14 represents such a dotted curve for a thick target with a maximum λ_{\max} above $2\lambda_0$.

The efficiency of X-ray production can be approximated for the continuum by integrating Kramers' formula (1.11). In relation to the input power of the X-ray tube P , the continuous radiation carries only a very small part, which is given by the empirical relation

$$\eta_{\text{cont}} \approx 1 \times 10^{-9} ZU_0 \tag{1.13}$$

In practice, η values between 0.001 and 0.7% can be reached. Most of the input power is converted into heat and dissipated by water-cooling.

1.3.3 Polarization of X-Rays

A wave is called “linearly polarized” if it oscillates only in one direction perpendicular to the direction of its propagation. That means that only transversal waves can be polarized. Usually, an original beam of visible light and also of X-rays is not polarized because all the different light or X-ray photons irregularly oscillate in different directions. However, shortly after the detection of X-rays, it became known that X-rays can be polarized like visible light; that means the electric and magnetic field vector of special X-ray beams oscillate only in a certain direction perpendicular to the beam direction.

In 1904, Barkla discovered the polarization of X-rays, which were emitted from an X-ray tube in a particular direction. He showed that X-rays are linearly polarized if the X-ray beam is perpendicular to the electron beam of the X-ray tube [5]. In this case, the electric field vector only oscillates in the plane spanned by both beams. Furthermore, if X-rays are scattered from a paraffin block they are linearly polarized since it can be shown that a second block can scatter these X-rays only in a particular direction [1].

The polarization has given evidence for the wavelike character of X-rays and moreover for the transversal kind of X-ray waves. Much later, synchrotron radiation was shown to be linearly polarized in the plane of the storage ring. The polarization of X-rays can be used to reduce the spectral background and thereby to improve the detection limits in X-ray fluorescence analysis.

1.3.4 Synchrotron Radiation as X-Ray Source

The first synchrotrons were constructed by Edwin Mattison McMillan in the United States and by Vladimir Iosifovich in the former Soviet Union in 1945. Synchrotron radiation (SR) was discovered in 1947 by General Electric in New York [51] when a bright arc of visible light was observed for the first time at an electron accelerator. Its closed electron tube was partly covered by a transparent instead of an opaque coating so that radiation became visible. Today, SR is obtained from a storage ring in which charged particles like electrons are stored in several bunches and maintained at high constant velocity or kinetic energy. The particles come from the actual accelerator ring called booster where they are accelerated by electric fields to almost light velocity. The relativistic particles are forced into a fixed circular orbit by several strong magnets. They are accelerated radially by the magnetic fields and hereby produce a brilliant radiation. Extended descriptions can be found in the literature [52–57] and online in the Internet [58–61].

Originally, the first users of synchrotrons constructed such large accelerators for particle physics. These machines called colliders were applied to high-energy collisions, for example, of electrons and positrons, as a new branch of science. SR was regarded as an undesired loss of energy that had to be compensated. Only several years later, scientists used the highly brilliant radiation emerging from those machines and recognized its incomparable potential for research offered to physicists, chemists, geologists, physicians, biologists, engineers, and art historians. The benefits of SR in all disciplines of application are unequalled.

A synchrotron facility usually consists of an electron or positron source, a first linear accelerator, a second circular accelerator, called a booster-synchrotron, and a storage ring that consists of a metallic tube with circular and straight sections with a total length from some meters up to several kilometers (Figure 1.15). In the booster-synchrotron, the electrons are accelerated by high-frequency (HF) amplifiers or clystrons to nearly light velocity. Around the storage ring, several dipole magnets, so-called bending magnets (BMs), are

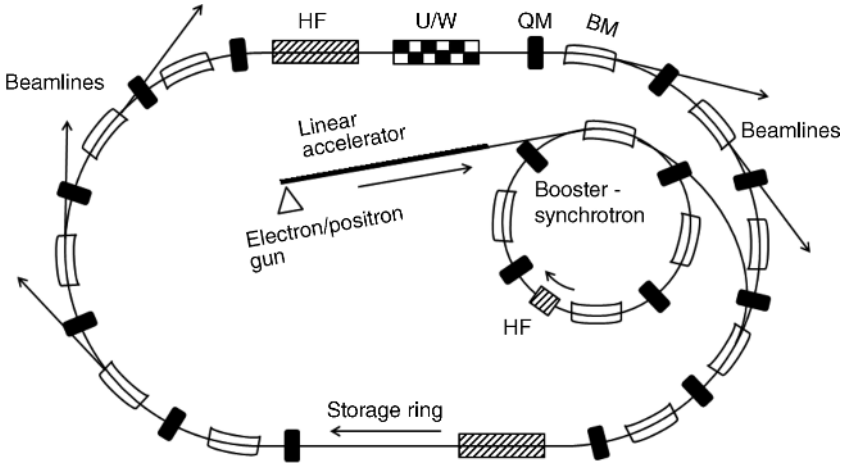


Figure 1.15. Schematic representation of a dedicated synchrotron facility. Essential parts are the electron or positron gun, the first linear accelerator, the second circular accelerator, called synchrotron or booster, the storage ring with a length of some 10 m up to several km. Different bending magnets (BM) and undulators or wigglers (U/W) are inserted for the production of the radiation. Quadrupole magnets (QM) are used for focusing the electrons. Several beamlines are arranged around the storage ring, always tangentially to the ring. A few electric HF fields provide energy in order to compensate for the radiation losses.

aligned, which force the electron beam into a fixed circular orbit. Furthermore, several quadrupole magnets (QMs) are used for focusing the electron beam again and again. The booster and the closed storage-ring are evacuated to ultra-high vacuum. Tangentially to the storage ring, several light pipes are attached at extra holes or switches and at the end of these beam lines different experiments are installed.

Electrons or positrons in the booster synchrotron come up to a relativistic velocity of more than $0.99999c$. Furthermore, they get a high mass connected with a high kinetic energy of more than 100 MeV. In the storage ring, the fast electrons or positrons do not get any additional kinetic energy. Within the curved parts of the ring, the electrons are deflected radially by magnetic fields on account of the Lorentz force and lose kinetic energy in the form of SR (see Section 3.3.1). In the linear or straight parts of the ring, undulators and wigglers (U/W) are inserted, which also deflect the charged relativistic particles and produce SR (see Section 3.3.2). This radiation emerges tangentially to the orbit of the relativistic electron or positron bunches within the beamlines. The energy loss caused by the radiation of the particles is compensated by HF amplifiers in some straight sections of the ring.

Synchrotron radiation is also emitted in the first accelerator or booster but it is only used for diagnostics. Single electron bunches from the booster are filled into the storage ring one after the other when they have reached a certain relativistic velocity or kinetic energy. In the ring, they build an electron beam

with bunches and gaps. This “train” uniformly rotates with almost light velocity in the ring. The temporary energy loss of the electrons according to the emitted SR is compensated again and again so that the original high velocity and kinetic energy of the electrons is kept constant here.

Synchrotron radiation covers a wide range of the electromagnetic spectrum from the infrared to hard X-rays with about eight orders of magnitude (see Figure 1.8). According to the electron or positron bunches, the radiation is pulsed. Furthermore, it is strongly collimated in a narrow cone in the forward pointing direction (fan with a vertical divergence of 0.1 mrad or 0.006° and a horizontal divergence of 5 mrad or 0.3°) and it is highly polarized. Linear polarization is ascertained in the orbital plane of the particles and elliptical polarization is observed at a small angle to that plane. Usually, a small bandwidth of the white radiation is selected to perform experiments with quasi-monochromatic radiation.

The scientific community using synchrotron light for spectrometry and diffractometry has been continuously growing since the 1970s. The high brilliance of SR sources exceeds that of conventional X-ray tubes by more than five orders of magnitude (see Section 3.3.3) and allows many experiments at the micro- and nanoscale with high lateral resolution and/or temporal resolution not known beforehand. Nowadays, synchrotrons are especially designed and constructed to produce this radiation. Facilities of the fourth generation will supply intense SR for a variety of experiments in a broad field of applications. The data (e.g., size and performance) of more than 60 machines spread over the whole world can be accessed online [60].

Synchrotron radiation is not only generated artificially by special electron accelerators but also appears naturally in astronomic objects. The radio emission of several galactic and extragalactic sources is caused by relativistic electron clouds trapped in strong magnetic fields. They can be found in jets of black holes, and in the nebulae of pulsars and quasars and can emit strong SR even in the X-ray region of the electromagnetic spectrum.

1.3.4.1 Electrons in Fields of Bending Magnets

Charged moving particles can be deflected in the magnetic field of a bending electromagnet. A particle with an electric charge q uniformly moving with a velocity \mathbf{v} in a homogeneous magnetic field \mathbf{B} is forced on a curved trajectory, for example, a circle, a spiral or a sinusoidal curve, by the so-called Lorentz force:

$$\mathbf{F} = q[\mathbf{v} \times \mathbf{B}] \quad (1.14)$$

All vectors are bold-faced and $[\mathbf{v} \times \mathbf{B}]$ is the cross-product of \mathbf{v} and \mathbf{B} .

For the synchrotron orbit spherical coordinates are chosen: r is the distance of a point from the center or origin (usually radius ρ_m), θ is the polar angle (between 0° and 2π or 360°), and ψ is the azimuthal angle of a position (0° within

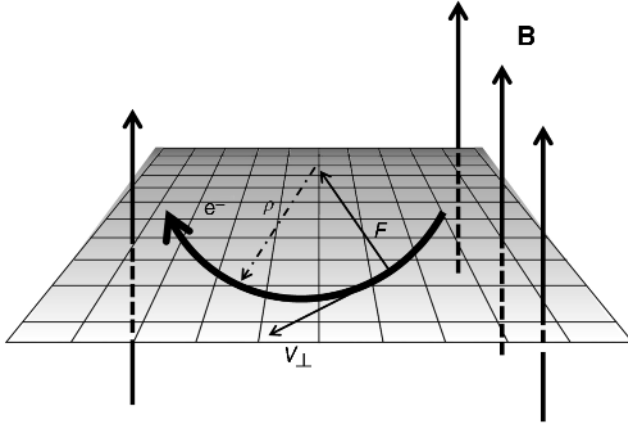


Figure 1.16. Trajectory of an electron e^- in a homogeneous magnetic field \mathbf{B} perpendicular to its velocity \mathbf{v} . The electron is deflected by the Lorentz force \mathbf{F} and moves uniformly on a circular orbit with radius ρ_m in the plane perpendicular to \mathbf{B} . The acceleration \mathbf{a} is always directed to the center of the circle and is vertical to \mathbf{B} . Consequently, a_{\parallel} is zero and a_{\perp} is the decisive quantity.

the orbit). The vectors \mathbf{v} and \mathbf{B} include the so-called pitch angle θ_p . If the magnetic field strength \mathbf{B} is perpendicular to the velocity \mathbf{v} , the pitch angle is $\pi/2$ or 90° , and the charged particle will move on a circular curve within a plane perpendicular to \mathbf{B} (Figure 1.16). The centripetal force for the particle and the Lorentz force can be set equal:

$$m_{\text{part}} \cdot \frac{v^2}{|\rho_m|} = q \cdot |\mathbf{v}| \cdot |\mathbf{B}| \tag{1.15}$$

where m_{part} is the mass of the particle and ρ_m is the radius of curvature of the circular orbit. Consequently, the radius can be calculated by

$$|\rho_m| = \frac{m_{\text{part}} \cdot |\mathbf{v}|}{q \cdot |\mathbf{B}|} \tag{1.16}$$

For relativistic atomic particles, Equation 1.15 has to be modified:

$$\frac{d}{dt} (m_{\text{part}} v) = q \cdot |\mathbf{v}| \cdot |\mathbf{B}| \tag{1.17}$$

The kinetic energy E_{part} and the particle mass are dependent on its relativistic velocity according to the Lorentz factor γ :

$$\gamma = \frac{m_{\text{part}}}{m_0} = \frac{E_{\text{part}}}{E_0} \tag{1.18}$$

where m_0 is the rest-mass of the particle and $E_0 = m_0 c_0^2$ is its rest-energy. With $\beta = v/c_0$ we get

$$\gamma = \frac{1}{\sqrt{1 - \beta^2}} \quad \text{and relatedly} \quad \beta = \sqrt{1 - \frac{1}{\gamma^2}} \quad (1.19)$$

Equation 1.17 can be rewritten as

$$\frac{d}{dt}(\gamma m_0 v) = q \cdot |v| \cdot |B| \quad (1.20)$$

Differentiation of the left-hand side leads to

$$m_0 \frac{d}{dt}(\gamma v) = m_0 \gamma a + m_0 \gamma^3 v \frac{(v \cdot a)}{c^2} \quad (1.21)$$

where a is the acceleration of the particle defined by dv/dt . If v is perpendicular to B , a is perpendicular to v . Consequently, the scalar product $v \cdot a$ vanishes and we get

$$m_0 \cdot \gamma |a| = q \cdot |v| \cdot |B| \quad (1.22)$$

For electrons or positrons, q is the elementary charge of about 1.602×10^{-19} C, m_0 is about 9.109×10^{-31} kg, and E_0 is nearly 511 keV. Table 1.6 gives typical β values for relativistic electrons, the corresponding

TABLE 1.6. Increasing β Values of Accelerated Electrons, their Lorentz Factor γ , their Energy and Mass, the Difference of their Velocity and the Light Velocity, and the Critical Energy of Emitted Photons

β	γ	E_{el} [MeV]	m_{el} [10^{-31} kg]	$(v - c_0)$ [m/s]	E_{crit} [eV]
0.1	1.005	0.514	9.2	-2.7×10^7	9×10^{-8}
0.9	2.294	1.172	21	-3.0×10^6	1×10^{-6}
0.95	3.203	1.637	29	-1.5×10^6	3×10^{-6}
0.99	7.089	3.622	65	-3.0×10^5	3×10^{-5}
0.999	22.37	11.43	204	-29979	0.001
0.9999	70.71	36.13	644	-2998	0.03
0.99999	223.6	114.3	2037	-300	0.99
0.999999	707.1	361.3	6441	-30	31
0.9999995	1000	511.0	9109	-15	89
0.9999999	2236	1143	20369	-3.0	991
0.999999942 ^a	2936	1500	26746	-1.7	2243
0.99999999	7071	3613	64413	-0.3	31333

^aThis value is realized at the synchrotron facility DELTA of the TU Dortmund.

Lorentz factor, the energy and the mass of the electrons, and the difference between v and c . It can be recognized that γ , E_{el} , and m_{el} strongly increase with β while $v - c_0$ strongly decreases, that is, v approaches c_0 . The conditions for relativistic positrons are the same.

With help of Equation 1.18, with $q = e$, $v = \beta c_0$, and $E_0 = m_0 c_0^2$, the radius of curvature $|\rho_m|$ determined by Equation 1.16 can be converted into

$$|\rho_m| = \frac{\beta}{ec_0} \cdot \frac{E_{\text{el}}}{|\mathbf{B}|} \quad (1.23)$$

Since β is nearly constant in the booster and in the storage ring, this equation makes clear that the ratio of the kinetic energy and the strength of the magnetic field $E_{\text{el}}/|\mathbf{B}|$ must be constant in order to keep the radius of the trajectory constant and to fix the electron beam in a closed orbit. In the booster synchrotron, the field-strength has to be increased synchronously with the kinetic energy of the electrons. The name synchrotron is due to this condition. In the storage ring, $|\mathbf{B}|$ has to be kept constant because E_{el} should be constant.

1.3.4.2 Radiation Power of a Single Electron

The particles running in accelerators and storage rings undergo energy losses, which can be described combining the expression for the radiation rate of a relativistic particle with the expression for the acceleration of the particle in its orbit [52]. The acceleration, \mathbf{a} , is always perpendicular to \mathbf{v} and to \mathbf{B} . Consequently, its component \mathbf{a}_{\parallel} (parallel to \mathbf{B}) is zero and the particle does not gain kinetic energy. However, the component \mathbf{a}_{\perp} (perpendicular to \mathbf{B}) is not zero and determines the bending radius ρ_m of the electron trajectory, according to [58,62]

$$|\mathbf{a}_{\perp}| = \frac{q}{m} \cdot |\mathbf{B}| \cdot |\mathbf{v}| = \frac{v^2}{\rho_m} \approx \frac{c_0^2}{\rho_m} \quad (1.24)$$

Charged particles are deflected in the magnetic field according to \mathbf{a}_{\perp} in the direction of the guiding center of a circle with ρ_m , so they are retarded radially inward. Because of this fact they lose energy as a kind of relativistic “bremsstrahlung.”

The basic quantity for the radiation emerging from highly accelerated particles in perpendicular magnetic fields is the total radiation loss $(\Delta E/\Delta t)$. It is a power quantity measured as energy per unit time emitted as photons with undefined energies. For a single relativistic particle the total radiation loss is given by [58,62–64]

$$\left(\frac{\Delta E}{\Delta t}\right) = \frac{2}{3} \cdot \alpha_f \cdot \hbar \cdot \frac{\gamma^4}{c_0^2} \cdot |\mathbf{a}_{\perp}|^2 \quad (1.25)$$

For a singly charged particle, the quantity α_f is Sommerfeld's fine-structure constant, defined by

$$\alpha_f = \frac{1}{4\pi\epsilon_0} \cdot \frac{e^2}{\hbar c_0} \quad (1.26)$$

where ϵ_0 is the electric field constant, and $\hbar = h/2\pi$ is the reduced Planck constant. α_f is dimensionless and amounts to $1/137$. It determines the power of the electromagnetic interaction and is a measure of the probability for a photon to be coupled to an electron or positron. Consequently, it is decisive for the emission rate that equals the radiation loss ($\Delta E/\Delta t$).

For relativistic particles with $v \approx c_0$ and $\beta \approx 1$, we find from Equation 1.25 by use of Equations 1.23 and 1.24

$$\left(\frac{\Delta E}{\Delta t}\right) = \frac{2}{3} \cdot \alpha_f \cdot \hbar \cdot \left(\frac{c_0}{\rho_m}\right)^2 \gamma^4 = \frac{2}{3} \cdot \alpha_f \cdot \hbar \cdot \frac{q^2 E_{\text{el}}^2 |\mathbf{B}|^2}{m_0^4} \quad (1.27)$$

These equations show that the radiation loss induced by a single electron is dependent on $1/|\rho_m|^2$ and on γ^4 , E_{el}^2 , $|\mathbf{B}|^2$, and $1/m_0^4$. Large values of γ , E_{el} , and $|\mathbf{B}|$ lead to the high photon fluxes of synchrotron radiation while small values of $|\rho_m|$ and of m_0 also effect a strong radiation. Because of their low rest-mass, the radiation power for electrons is 10^{13} times stronger compared with that for protons. That is the reason why electrons or positrons are used as sources for synchrotron radiation in preference to protons or α particles. A single electron or positron causes power values of $>10^{-7}$ W. All electrons together in a beam of some 100 mA yield a radiation energy of some 30 kW [63].

1.3.4.3 Angular and Spectral Distribution of SR

The trajectory of charged particles crossing a homogeneous field is an arc of a circle as already demonstrated in Figure 1.16. The geometry of the radiation emitted by relativistic electrons observed in the rest frame of the relativistic electron, S' , is that of a dipole. The angular distribution of the radiation with respect to the velocity vector in S' is

$$I_v \propto \sin^2\theta' = \cos^2\Delta\theta' \quad (1.28)$$

where θ' is the horizontal emission angle and $\Delta\theta'$ is its complement to $\pi/2$ or 90° . I_v gives the probability distribution of photons that are emitted from a dipole leading to the isotropic dipole pattern of this figure with a width of π or 180° .

The aberration between this rest frame S' and the reference or laboratory frame S can be described by [58,62]

$$\sin \Delta\theta = \frac{1}{\gamma} \frac{\sin \Delta\theta'}{1 + \beta \cos \Delta\theta'} \quad \text{and} \quad \cos \Delta\theta = \frac{\cos \Delta\theta' + \beta}{1 + \beta \cos \Delta\theta'} \quad (1.29)$$

At the angles $\theta' = \pm\pi/2$, the intensity of the emitted radiation is zero in S' . According to Equation 1.29, the corresponding angles in S meet the condition of $\sin \Delta\theta = \pm 1/\gamma$ and $\cos \Delta\theta = \beta$. Consequently, $\Delta\theta$ is about $\pm 1/\gamma$. The radiation is beamed in the direction of the particles motion within $-1/\gamma < \Delta\theta < +1/\gamma$. It leads to the forward-pointing narrow cone of Figure 1.17 where the observation line and the velocity vector of the accelerated particles coincide within a horizontal emission angle of about $2/\gamma$. This is also valid for the vertical emission angle. The higher the speed of the electrons, the narrower the momentary emission cone of the photons become. Within a certain time interval the cone describes a fan that may be 10 times wider.

The emitted radiation of a single relativistic electron is a flux with a large number of photons. They all do not have the same energy but carry very

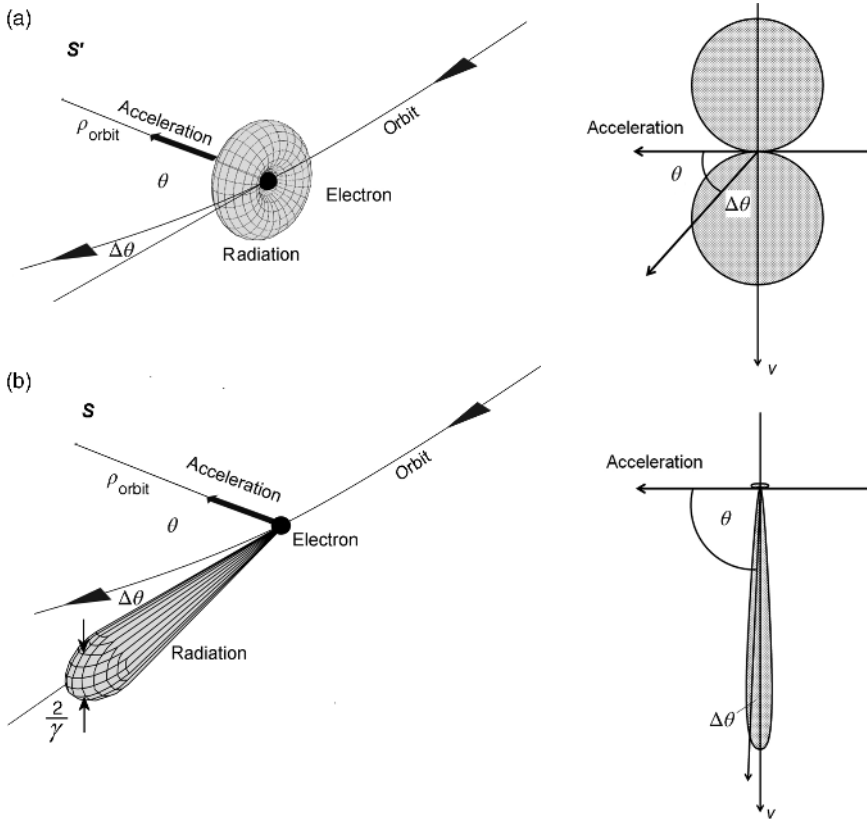


Figure 1.17. The emitted radiation of relativistic electrons deflected by a homogeneous magnetic field \mathbf{B} vertical to the orbit plane. The rest frame S' of the electron (a) shows an isotropic dipole pattern while the relativistic frame S of the observer (b) gives a narrow cone in forward direction. Three-dimensional view (left). Cross-section of the orbit plane (right). θ and $\Delta\theta$ are emission angles between velocity \mathbf{v} and Lorentz force \mathbf{F} or acceleration \mathbf{a} . Its sum is 90° or $\pi/2$. Figure from Ref. [53], reproduced with permission from K. Wille.

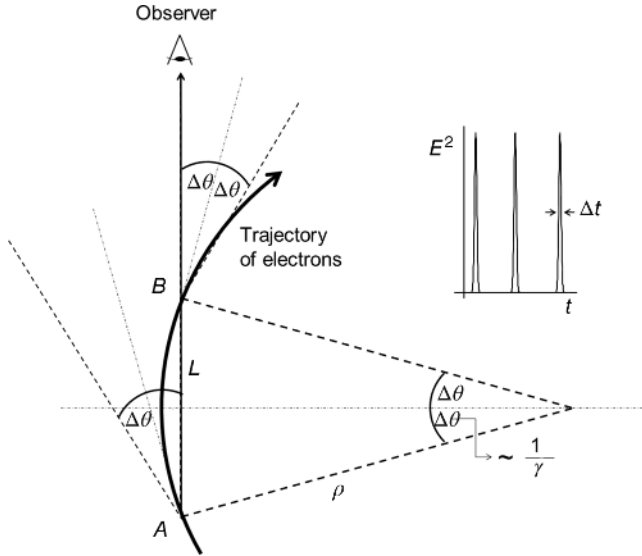


Figure 1.18 Observation of photons emitted from a relativistic electron by its deflection in a perpendicular magnetic field. The first photon emitted from point A moves to point B on the secant with length L at light velocity. The last photon is emitted from point B after the electron has covered the arc AB with the velocity v . The observer detects an ultrashort radiation pulse with length Δt , which is equal to the difference between the time of flight of the electron and the photon. L is about 2 mm, $\Delta\theta$ is about 0.02° , and the bunch length is some centimeters. Figure from Ref. [53], reproduced with permission from K. Wille.

different photon energies. This spectral nature of the relativistic radiation emitted at a bending electromagnet in a storage ring can be illustrated in a simple way [52,53,63]. As demonstrated in Figure 1.18, a single electron moves on an arc of a circle with the velocity $v = \beta c_0$ within a horizontal emission angle $2\Delta\theta = 2/\gamma$. An observer tangential to the ring will record a first photon emitted from point A. The first photon runs from A to B on the secant of the circle with the horizontal emission angle. Simultaneously, the electron moves from A to B on the corresponding arc of that circle and emits the last photon from point B. After that, both photons reach the observer on a straight line.

The duration of the electromagnetic pulse recorded by the observer is the time difference between both photons. It is identical to the difference between the time of flight of the electron and of the first photon, in both cases from A to B, on the condition that the electron runs behind the photon with $v < c$. According to Longair [62] and Weis *et al.* [63], the pulse length caused by the photons is approximately

$$\Delta t \approx L \left(\frac{1}{v} - \frac{1 - 1/6\Delta\theta^2}{c_0} \right) \quad (1.30)$$

where L is the secant of the circle or the distance between A and B . This quantity can be estimated to

$$\Delta t \approx \frac{4\rho_m}{3c_0} \cdot \frac{1}{\gamma^3} \quad (1.31)$$

which is typically of the order of 10^{-18} s down to 10^{-20} s, that is, the photon pulses are ultrashort. After the mentioned electron, the next electron of the bunch will produce the next pulse. Altogether some 10×10^{12} (some 10 billion, Europe; and some 10 trillion, US and UK) of electrons typically belong to a bunch and participate in the emission of photons. The distance of electrons is about some pm, while the secant of the electron orbit being observed is some mm.

Usually, many bunches of electrons or positrons (up to some hundred) are grouped in a storage ring separated by just as many gaps. The bunch length is some cm, the gaps or empty parts are about 50 times longer, and the storage ring may typically have a circumference of some 100 m. The chain of bunches with the electrons rotate within the ring like a train with nearly light velocity. They rotate with the gyrofrequency $\omega = c_0/\rho_m$, also called Larmor frequency, which amounts to about 100 MHz for magnets with a bending radius of 3 m. The electrons of a bunch induce the emission of photons with a period of some 10^{-20} s, the photons recorded by an observer cause an electronic pulse of some 10^{-19} s, a bunch emits photons during some 10^{-11} s, the bunches follow each other after some 10^{-9} s. They cross the homogeneous magnetic field within some 100 ns up to 100 μ s and yield a beam current of some 100 mA.

According to Wille [53], the radiation pulses have first to be corrected for effects of aberration and time retardation. Afterward, a Fourier transformation for the pulses has to be carried out in order to get the spectrum of this radiation. In accord with Heisenberg's relation, the very short pulses of some 10^{-19} s give a spectrum with a broad bandwidth, $\Delta E = h/\Delta t$, which amounts to nearly 10 keV. The spectral photon flux ($\Delta W/\Delta E$) dependent on the energy of the emitted photons was first derived from theory by Schwinger [54] as mentioned in [53,58,62]. In order to compare the results with the spectra used in energy-dispersive X-ray spectrometry, the photon energy was chosen here as the variable quantity instead of the wavelength or the frequency. The calculation is discussed in detail (e.g., by Jackson [65] and Hoffmann [66]) leading to the expression

$$\left(\frac{\Delta W}{\Delta E}\right) = \sqrt{3} \cdot \alpha_f \cdot \gamma \cdot x \cdot \int_x^\infty K_{5/3}(\xi) d\xi \quad (1.32)$$

where x is the photon energy E related to E_{crit} , which will be defined later. $K_{5/3}$ is a modified Bessel function of the fractional order $5/3$; its integral goes from $x = E/E_{\text{crit}}$ up to ∞ . This basic quantity ($\Delta W/\Delta E$) is dimensionless and can be converted into the number of photons per electron. It is usually standardized to

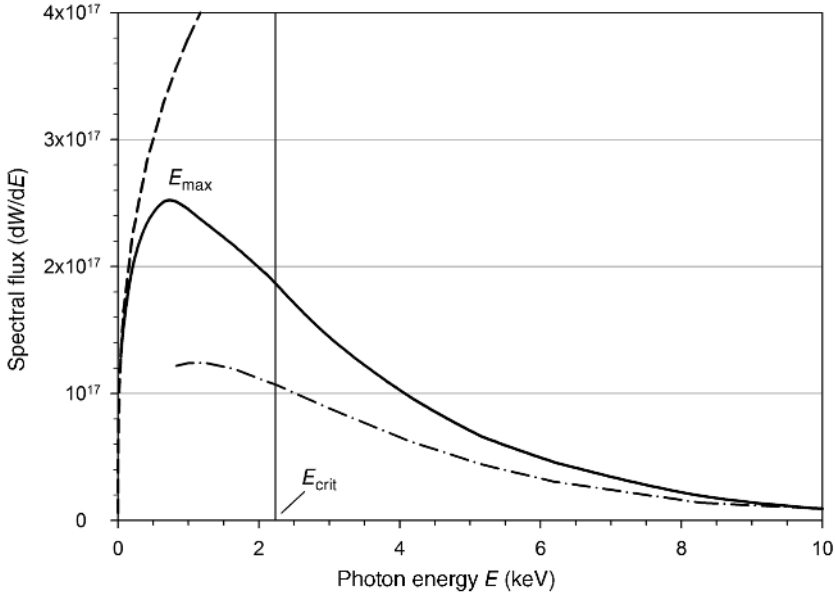


Figure 1.19. Typical continuous spectrum of synchrotron radiation. The spectral flux (dW/dE) is dependent on the energy E of the emitted photons. It is given as a dimensionless quantity in arbitrary units. The energy E_{el} of the relativistic electrons in the storage ring was chosen to be 1.5 GeV (DELTA at the TU-Dortmund) so that the critical energy E_{crit} was 2.24 keV. The area below the curve for $E \leq E_{crit}$ is equal to the area for $E \geq E_{crit}$. Two asymptotic approximations are presented: for low photon energies (dashed curve) and for high photon energies (dashed-dotted).

an electron beam current of 1 Ampere with 6.242×10^{18} electrons per second (trillions, Europe; or quintillions, US and UK) and to a spectral bandwidth of 0.1% (that means a bandwidth ΔE of 1 eV at $E = 1$ keV).

The radiation is emitted in a narrow cone and shows a bell-shaped distribution, which is dependent on the observation angle in the horizontal orbit plane and in the vertical plane. The flux shows a maximum for in-plane and on-axis and is usually given for in-plane ($\psi = 0$) or it is averaged by integration over the vertical divergence $\Delta\psi$. A typical distribution is demonstrated in Figure 1.19 for a small synchrotron facility. It shows a linear plot of the averaged spectral flux dependent on the energy of the emitted photons. The black curve looks like a broad hump with an increasing and a decreasing branch. The photon energy, which divides the area below the curve into two equal parts, is denoted as the critical (or characteristic) energy. Half the flux is emitted for $E \leq E_{crit}$, the other half presents energies $E \geq E_{crit}$. The critical energy is given by

$$E_{crit} = \frac{3}{2} \cdot \hbar \cdot \frac{c_0}{\rho_m} \cdot \gamma^3 \quad (1.33)$$

Different values for E_{crit} have already been listed in Table 1.6 provided that the bending radius is chosen to be 3.34 m (at DELTA in Dortmund).

The integral of the Bessel function in Equation 1.32 can be approximated for two special cases. For small energies ($E \ll E_{\text{crit}}$) of the emitted photons, the increasing branch can be written as

$$\left(\frac{\Delta W}{\Delta E}\right) \cong \frac{11}{9} \cdot \pi \cdot \alpha_f \cdot \gamma \cdot \left(\frac{E}{E_{\text{crit}}}\right)^{1/3} \quad (1.34)$$

For high energies ($E \gg E_{\text{crit}}$) of photons, the decreasing branch is

$$\left(\frac{\Delta W}{\Delta E}\right) \cong \frac{2}{3} \cdot \pi \cdot \alpha_f \cdot \gamma \cdot \left(\frac{E}{E_{\text{crit}}}\right)^{1/2} \cdot \exp\left(-\frac{E}{E_{\text{crit}}}\right) \quad (1.35)$$

Both asymptotes were calculated and also presented in Figure 1.19 as dimensionless quantities (Watt/Watt). It can simply be shown that Equation 1.35 has a maximum at $0.50 E_{\text{crit}}$ and reaches a spectral flux ($\Delta W/\Delta E$) with a value of about $0.9 \alpha_f \gamma$. The maximum of the actual curve in black, however, is located at $E_{\text{max}} \approx 0.29 E_{\text{crit}}$ [52,53] with a value of nearly $1.8 \alpha_f \gamma$ according to Equation 1.32.

As stated, the basic quantity of SR is the spectral flux, which can be given by the number of photons with a certain energy emitted per unit time or second. Usually a bandwidth of 0.1% of the respective average energy is chosen while the beam current is normalized to 1 ampere and the electron energy is assumed to be 1 GeV. However, for local investigations it is decisive that the radiation source is a spot with a very small angular divergence. For that reason, the flux is related to the respective solid angle and is called angular density of the flux or spectral brightness [53]. When the photon flux is related to a small source area (cross-section of the beam) in addition, it is called brilliance [56]. These quantities are commonly used in the synchrotron literature though brilliance is also called spectral brightness in English-speaking areas (USA, UK). Brilliance is mostly related to number of photons per second, per mrad^2 , per mm^2 , and per 0.1% spectral bandwidth but *not* to the SI units of 1 sr and of 1 m^2 [67].

Figure 1.20 represents the brilliance derived from Figure 1.19 in a double logarithmic plot with both asymptotic approximations. It represents the *average* brilliance integrated over the small vertical divergence. For low photon energies, we find an increasing straight line with the slope $1/3$;¹ for high photon energies, we have a decreasing exponential curve. A comparison with the radiation of a black body is described later.

¹ In comparison to the average brilliance with a slope of $1/3$ for the increasing branch, the in-plane brilliance shows a slope of $2/3$ and a maximum which is nearly doubled.

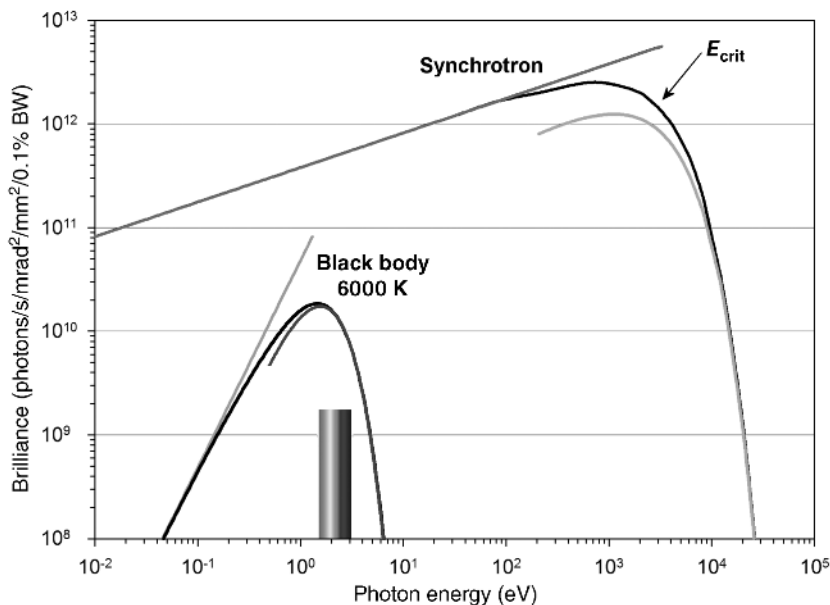


Figure 1.20. The continuous spectrum of Figure 1.19 as a double-logarithmic plot. The ordinate was converted into the brilliance or number of photons/s/mrad²/mm²/0.1% bandwidth, respectively. Again, the two asymptotes are presented for low and for high photon energies (red straight line and blue curved line). The range of transition is marked in black, the maximum is at $0.29 E_{\text{crit}}$. For comparison, the photon flux of a black-body is plotted according to Planck's law. At a temperature $T = 6000$ K, the black curve on the left shows a maximum at $E_{\text{max}} \approx 1.5$ eV in the visible color-coded region. (See colour plate section)

Synchrotron radiation shows a dependence on the kinetic energy, E_{el} , of the beam electrons. If the electron energy is increased synchronously with the magnetic field, the radius of the electron orbit is held constant—as already mentioned earlier. The result for the photon flux is illustrated in Figure 1.21. There is no change of the flux on the low-energy side, but with higher electron energies, the curves grow and are shifted to the right, that is, to the high-energy side. The positions E_{max} are shifted according to $0.29 E_{\text{crit}}$ and the maxima are increased proportional to E_{el}^2 . It may be mentioned that two parts of radiation appear: one part oscillating parallel to the magnetic field and the other part perpendicular to it. It can be shown that the perpendicular part is seven times larger than the parallel one [52,58,68]. Further details of SR facilities especially with undulators, wigglers, and free-electron lasers are given in Section 3.3.2.

1.3.4.4 Comparison with Black-Body Radiation

Because of the excellent properties of SR, storage rings can even serve as radiation standards like the European calibration standard for electromagnetic radiation, MLS, in Berlin, Germany. The continuous spectrum of SR is of relativistic origin

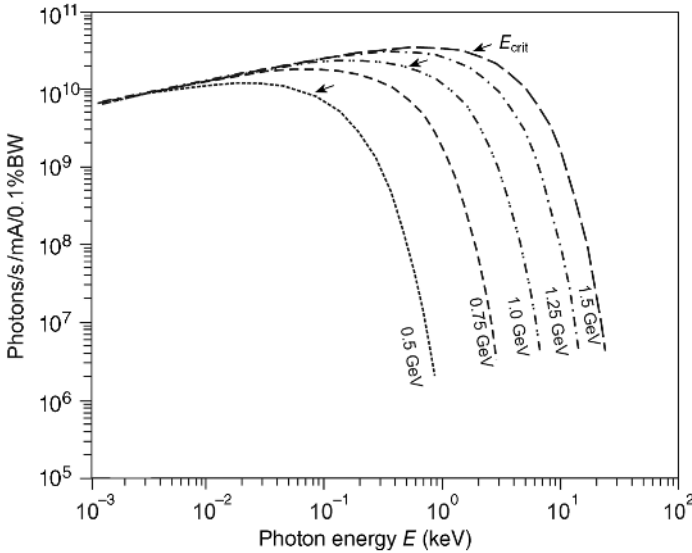


Figure 1.21. Spectral flux of synchrotron radiation depending on the photon energy as a double logarithmic plot. When the kinetic energy of the electrons or the beam energy is increased from 0.5 to 1.5 GeV in steps of 0.25 GeV, the curves rise and move to the high-energy side. The maxima occur at $0.29 E_{crit}$ and are shifted from 0.024 to 0.64 keV in four different steps. The curves were calculated after Equations 1.34 and 1.35, linked together and scaled for DELTA in Dortmund.

but resembles the thermal radiation of a black body (BB). Both, the continuous spectrum of SR and the “white” spectrum of BB can be calculated with sufficient accuracy in contrast to the continuous spectrum of an X-ray tube.

A black body is in thermodynamic equilibrium and characterized by its temperature T , in Kelvin. It emits electromagnetic radiation, which is homogeneous, isotropic, and unpolarized. The spectral power ΔP is given by Planck’s law usually expressed in terms of frequency ν , or wavelength λ , or the reciprocal value $1/\lambda$, called wavenumber [69]. In order to compare both radiation sources, this law was adapted to a function of the energy $E = h\nu$ of emitted photons:

$$\Delta P(E, T) = 2c_0 \cdot \left(\frac{E}{hc_0}\right)^3 \cdot \frac{\Delta A \Delta \Omega \Delta E}{\exp\left(\frac{E}{kT}\right) - 1} \tag{1.36}$$

where h is Planck’s constant and k is Boltzmann’s constant ($hc_0 = 1.2398 \times 10^{-6}$ eV·m and $k = 8.617 \times 10^{-5}$ eV/K). The infinitesimal quantity $\Delta P(E, T)$ is determined as the power in Watt for photons with energy in eV. It is radiated normally from the surface of the BB with an area ΔA , into a solid angle of detection $\Delta \Omega$, within an energy band ΔE , centered on E . For a comparison with SR, ΔP has been related to an energy band set to 0.1% of the relevant photon energy. ($\Delta P/\Delta E$) can be calculated in Watt per Joule or can be converted into the number of photons

emitted per second in the relevant energy band. Differentiation shows that the distribution ($\Delta P/\Delta E$) peaks at E_{\max} of nearly $3kT$ (more exactly at $2.82kT$). This is in full agreement with Wien's displacement law $E_{\max} = b \cdot T$ where $b \approx 2.431 \times 10^{-4}$ eV/K. The maximum itself amounts to about $c_0(E_{\max}/2hc_0)^3 \Delta A \Delta \Omega$.

Again two approximations can be deduced. For photons with low energies ($E \ll kT$), the law of Rayleigh–Jeans is valid:

$$\frac{\Delta P(E, T)}{\Delta E} = 2c_0 \cdot \left(\frac{E}{hc_0}\right)^3 \cdot \frac{kT}{E} \Delta A \Delta \Omega \quad (1.37)$$

For photons with high energies ($E \gg kT$), the approximation of Wien can be used:

$$\frac{\Delta P(E, T)}{\Delta E} = 2c_0 \cdot \left(\frac{E}{hc_0}\right)^3 \cdot \exp\left(-\frac{E}{kT}\right) \Delta A \Delta \Omega \quad (1.38)$$

Planck's law is presented in Figure 1.20 for a black body with a temperature of 6000 K in addition to the synchrotron curves. Source area and solid angle of the BB radiation were assumed to be as large as for SR with $\Delta A = 1.75 \times 10^{-2}$ mm², and $\Delta \Omega = 0.17$ (mrad)². It can be read from the curves that the continuum of BB is similar to the continuum of SR with a strong exponentially decreasing branch, but BB shows a steeper increasing branch with a slope of 2 instead of 1/3. The black body at 6000 K mainly radiates in the visible region indicated by a colored ribbon.

1.4 ATTENUATION OF X-RAYS

Different phenomena have to be considered as forming the basis of X-ray spectrometry; the attenuation of X-rays as well as their deflection and diffraction. These phenomena result from the interaction between radiation and matter and can be described partly by the wave picture and partly by the corpuscle picture as already mentioned earlier.

If an X-ray beam passes through matter, it will lose intensity due to different effects. According to Figure 1.22, the number of photons N_0 hitting upon a homogeneous sheet or layer of density ρ and thickness d is reduced to a fraction N being transmitted while the difference, $\Delta N = N_0 - N$, has been lost. Generally, the attenuation of intensity is controlled by the Lambert–Beer law. This law can be written either in the differential form

$$\frac{\Delta N}{N} = -\left(\frac{\mu}{\rho}\right) \rho \Delta d \quad (1.39)$$

or in the integral form

$$N(d) = N_0 \exp\left[-\left(\frac{\mu}{\rho}\right) \rho d\right] \quad (1.40)$$

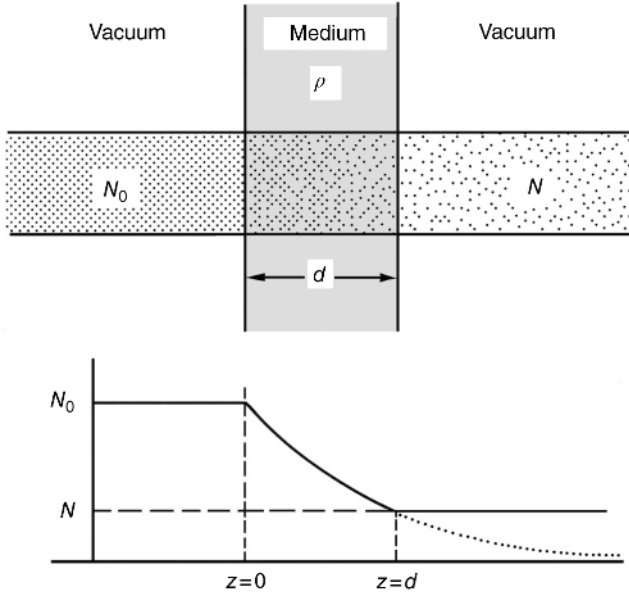


Figure 1.22. Attenuation of an X-ray beam penetrating through a homogeneous medium of density ρ and thickness d . The number of photons is reduced exponentially from N_0 to N . After Ref. [8], reproduced with permission. Copyright © 1996 by John Wiley and Sons.

where μ is the linear attenuation coefficient, and (μ/ρ) is called the mass-attenuation coefficient defined by the Lambert–Beer law in Equation 1.11. The intensity exponentially depends on the thickness of the layer and will be reduced to $1/e$ or nearly 37% if, for example, X-ray photons of about 20 keV pass through metal sheets of medium density with about 10–200 μm thickness.

The mass-attenuation coefficient expressed in cm^2/g is a quantity that depends on the element composition of the material and the energy of the X-ray photons. Since the density is incorporated, (μ/ρ) is independent of the state of aggregation. Values for a solid, liquid, or gas, whether it is a compound, solution, or mixture, will be equal if the composition of the material is equal. For the sake of clarity, this notation is preferred here. Some authors only use μ instead of the product, $(\mu/\rho)\rho$, for simplicity; others choose the symbol μ instead of (μ/ρ) .

The mass-attenuation coefficient follows an additive law so that values of a compound, solution, or mixture can readily be calculated from values of the individual elements if the element composition is known:

$$\left(\frac{\mu}{\rho}\right)_{\text{total}} = \sum c_i \left(\frac{\mu}{\rho}\right)_i \tag{1.41}$$

where the values of c_i are the mass fractions of the different elements present in the total mixture. Of course, the individual coefficients, $(\mu/\rho)_i$, are

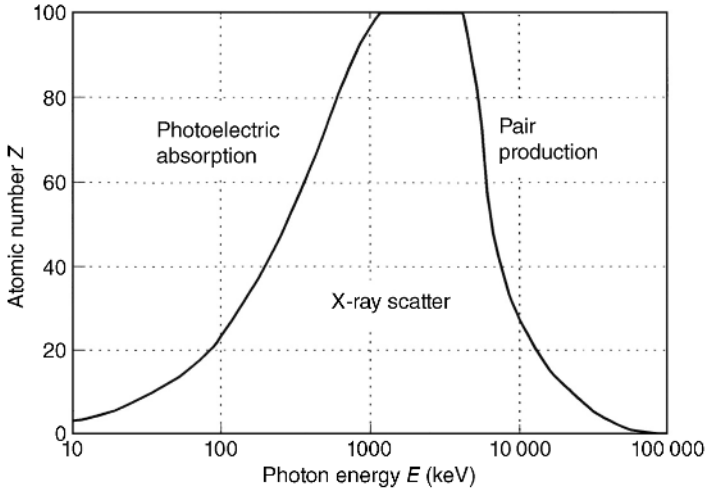


Figure 1.23 Isofrequency lines and predominant effects for the attenuation of X-rays in material of atomic number Z plotted against the photon energy E . Figure from Ref. [71], reused with permission from Springer Science + Business Media.

functions of the energy of the X-ray photons, so that the total value is determined only for X-ray photons of a certain energy, that is, for a monoenergetic X-ray beam. The individual values for each element and for several energies of X-ray photons can be taken from tables (e.g., from Bertin [48] or Tertian and Claisse [50] or the Internet [61]) or can be calculated using functions (e.g., given in Ref. [70]).

The attenuation of X-rays is caused by the interaction of their photons with the inner or the outer electrons, or even with the nuclei of atoms. It results from three competing effects, called photoelectric absorption, X-ray scatter, and pair production. As indicated in Figure 1.23 [71], the photoelectric effect predominates for E below 100 keV and is the most important in X-ray spectroscopy. Pair production does not occur for E smaller than 1 MeV, so it is insignificant for X-ray spectroscopy and will not be considered further here.

1.4.1 Photoelectric Absorption

The major component of X-ray absorption is caused by the photoelectric effect by which an electron of an inner shell of an atom is expelled by a photon of sufficient energy. The primary photon itself is completely annihilated while a secondary photon of lower energy is emitted immediately after the rearrangement of electrons. The *secondary emission* is called X-ray fluorescence (already described in Section 1.3.2.1).

Photoelectric absorption is evaluated numerically by a specific mass-absorption coefficient (τ/ρ) . It can be considered as the sum of all possible expulsions of electrons from the various atomic shells K, L, M, N, O, and P, and consequently is determined by

$$(\tau/\rho) = (\tau/\rho)_K + (\tau/\rho)_L + (\tau/\rho)_M + (\tau/\rho)_N + (\tau/\rho)_O + (\tau/\rho)_P \tag{1.42}$$

The different additive parts can further be split up according to the corresponding subshells. All the individual coefficients approximately follow the Bragg–Pierce law:

$$\left(\frac{\tau}{\rho}\right)_j = k_j Z^3 / E^{8/3} \tag{1.43}$$

with different constants k_j of the different subshells or levels j . In a double logarithmic plot of (τ/ρ) versus E presented in Figure 1.24, the linear segments show a negative slope of $-8/3$ and are mutually parallel. At the absorption edges, abrupt jumps of (τ/ρ) appear because further electrons of the next outer shell can be expelled if the photon energy exceeds the corresponding edge energy. For higher energies, the mass-absorption

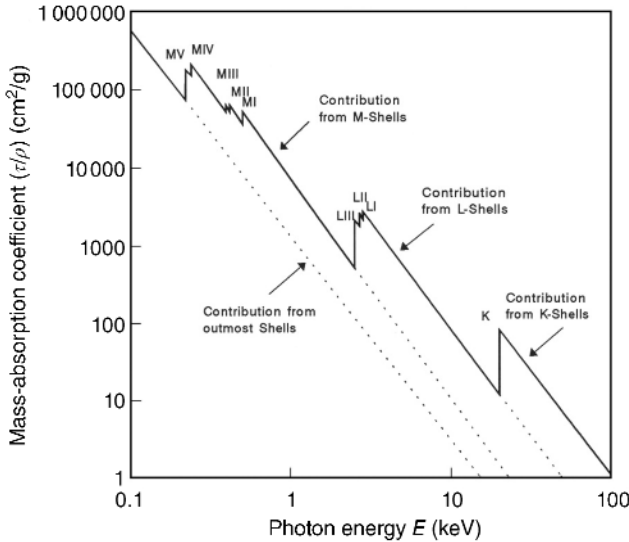


Figure 1.24. Total photoelectric mass-absorption coefficient (τ/ρ) for molybdenum vs. the photon energy E . Each discontinuity corresponds to an additional photoelectric process that occurs if the respective absorption edge K, $L_I \dots L_{III}$, or $M_I \dots M_V$ is exceeded or jumped over. Data from Ref. [48], reproduced with permission from Plenum Press.

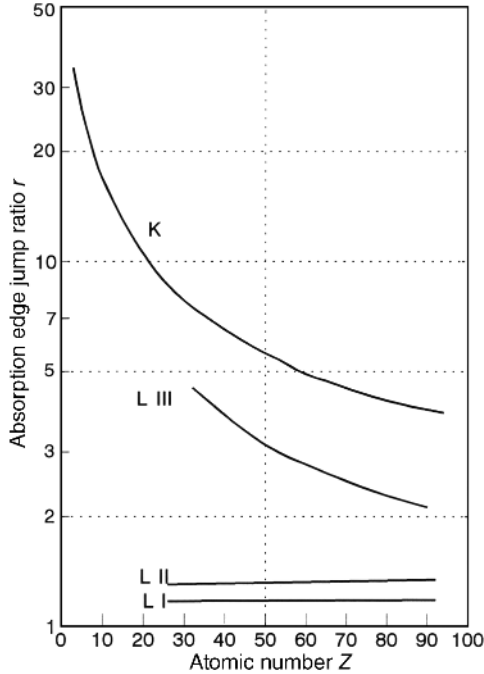


Figure 1.25 Absorption-edge jump ratio r for K, L_I, L_{II}, and L_{III} edges plotted against the atomic number Z of the material. Figure from Ref. [48], reproduced with permission from Plenum Press.

coefficient gradually falls again with the slope $-8/3$. The specific edge energies correspond to the binding or ionization energies of electrons in the respective shells or subshells. They follow the extended Moseley's law of Equation 1.6. The respective characteristic emission peaks always lie at somewhat lower energies (see Section 1.3.2.1).

The jump ratio at an absorption edge is defined by the quantity

$$r_j = \frac{(\tau/\rho)_{\text{high}}}{(\tau/\rho)_{\text{low}}} \quad (1.44)$$

where the subscripts “high” and “low” refer to the high- and low-energy side of an edge. The jump ratios of the K and L edges are represented in Figure 1.25 for various elements. From the jump ratio, another useful quantity can be derived called the absorption jump factor f_j . It is defined as the fraction $(\tau/\rho)_j$ of a certain shell or subshell j with respect to the total value (τ/ρ) according to

$$f_j = \frac{(\tau/\rho)_j}{\Sigma(\tau/\rho)_j} \quad (1.45)$$

Jump factor and jump ratio are correlated according to

$$f_j = \frac{r_j - 1}{r_j} \quad (1.46)$$

1.4.2 X-Ray Scatter

The second and generally minor component of X-ray absorption is caused by the scattering of X-ray photons. In contrast to photoelectric absorption, the primary photons do not ionize and excite an atom or molecule but are only deflected from their original direction. Three processes can be distinguished:

1. The collision of a photon with a firmly bound inner electron of an atom can lead to a change of direction of the photon without energy loss. This process is called *elastic scattering* or *Rayleigh scattering*.
2. The collision of a photon with outer electrons of molecules can also lead to a deflection and additionally, in a very few cases (1 in 10 million), to a change of its energy. The photons can win or lose energy in discrete steps or continuously in a wide band. The effect is called *inelastic Raman scattering*.
3. The collision of a photon with a loosely bound outer electron of an atom or molecule or even with a free electron can lead to a change of direction *and* a loss of energy of the photon. This process is called *inelastic scattering* or *Compton scattering*. A strict relationship exists between energy loss and angle of deflection.

Generally, the photons can be deflected in all directions. Rayleigh and Raman scattering can be coherent, that is, there is a fixed relation of phases for the incident and the scattered photons. By way of contrast Compton scattering is always incoherent. Rayleigh scattering occurs at crystal planes or multilayer interfaces (Section 2.3.5). Raman scattering is mainly concerned with the translation and rotation of molecules in gases, and spectra are observed in the visible and moreover in the infrared region.

In the corpuscle picture, the loss of *energy* a photon suffers in Compton scattering results from the conservation of total energy and total momentum at the collision of the photon and the electron. A photon with the initial energy E keeps the part E' when it is deflected by an angle ψ , while the electron takes off the residual part of energy $dE = E - E'$. The fraction E'/E can be calculated according to

$$E'/E = [1 + (1 - \cos \psi)E/E_0]^{-1} \quad (1.47)$$

where E_0 is the rest energy of an electron which amounts to 511 keV. Figure 1.26 represents the distribution of E'/E for any given direction ψ in

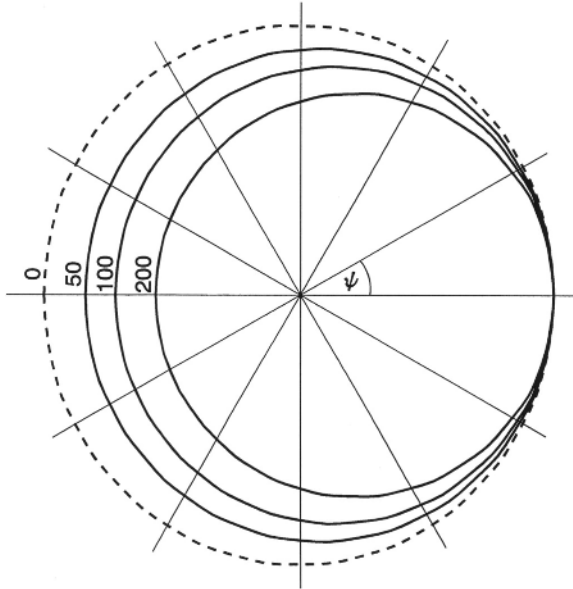


Figure 1.26. Compton-scatter of a photon with an initial energy E . On collision with a loosely bound or free electron the photon is deflected by an angle ψ . It loses energy and keeps only the fraction E'/E . This fraction is represented by an ellipse in polar coordinates for a certain energy E (50, 100, and 200 keV). It may be compared with the outer dashed circle, representing conservation of the photon energy. Figure from Ref. [8], reproduced with permission. Copyright © 1996, John Wiley and Sons.

polar coordinates. The fraction depends on the initial energy but is independent of the substance of the scatterer. It shows maxima for $\psi = 0^\circ$ (forward scatter), reaches minima for $\psi = 180^\circ$ (backward scatter), and decreases with the initial energy.

In the wave picture, Compton scattering is controlled by a fixed wavelength shift, $d\lambda = \lambda' - \lambda$. It amounts to

$$d\lambda = \lambda_C \cdot (1 - \cos \psi) \quad (1.48)$$

where λ_C is a small constant called Compton wavelength, which is defined by $\lambda_C = h c_0/E_0 = 0.002426$ nm. The wavelength shift depends only on the deflection angle ψ and is independent of the wavelength λ itself. For $\psi = 0^\circ$, the shift is always zero, and for $\psi = 180^\circ$, it is always $2\lambda_C$, which is maximum.

The *intensity* of the scattered radiation shows a dependence on E and ψ , as shown in Figure 1.27 [72]. Minimum intensity or scattering is achieved for a deflection around 90° – 100° . For that reason, a rectangular geometric arrangement of the X-ray tube, sample, and detector is generally chosen in X-ray spectrometry in order to minimize the inelastic scatter into the detector. Nevertheless, any primary radiation of an X-ray tube is scattered by the sample and is reproduced as a blank spectrum. In particular, the characteristic peaks of

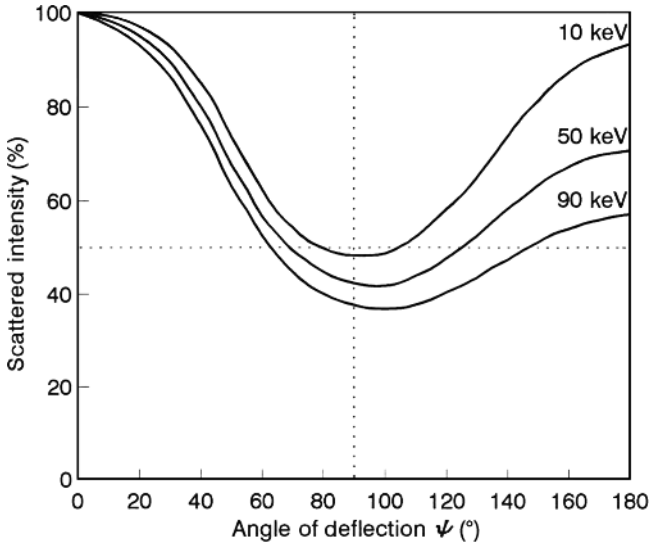


Figure 1.27. The normalized fraction of scattered *intensity*—Compton scatter—as a function of the angle ψ by which the incident photon is deflected after collision with an electron. Figure from Ref. [72], reproduced with permission from Thermo Fisher.

the tube anode give rise to the so-called Rayleigh and Compton peaks in a sample spectrum. Their corresponding *energies* can be calculated by Equation 1.47 for $\psi = 90^\circ$, independent of the sample itself. Their *intensities*, however, depend on the photon energy and moreover on the sample substance. Rayleigh scattering will increase if the energy of X-ray photons decreases or the mean atomic number of the scattering sample increases. Compton scattering, in contrast, will decrease if the photon energy decreases or the atomic number increases.

1.4.3 Total Attenuation

Photoelectric absorption and scattering jointly lead to the attenuation of X-rays in matter. The total mass-attenuation coefficient is composed additively by the photoelectric mass-absorption coefficient (τ/ρ) and the mass-scatter coefficient (σ/ρ) according to

$$(\mu/\rho) = (\tau/\rho) + (\sigma/\rho) \quad (1.49)$$

Both fractions are shown in Figure 1.28 for the element palladium, as functions of the photon energy [57,73]. The scatter coefficient is further divided into the Rayleigh and the Compton part. In contrast to the exponential decrease of (τ/ρ) with discontinuities at the absorption edges, the function (σ/ρ) varies more slightly and steadily. It decreases for Rayleigh scattering and increases for

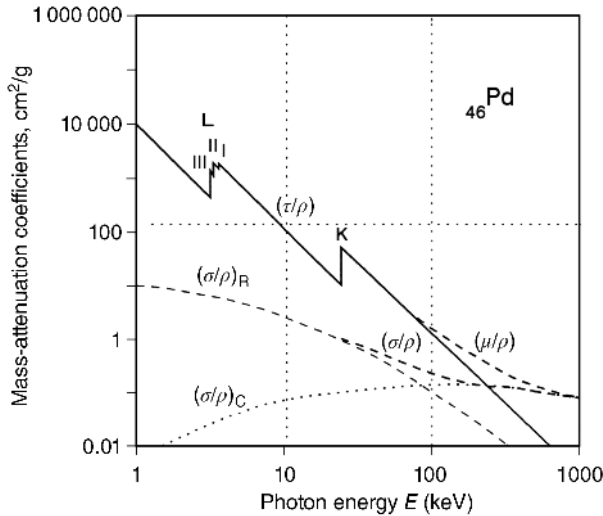


Figure 1.28. Photoelectric mass-absorption coefficient (τ/ρ) and mass-scatter coefficient (σ/ρ) as functions of the energy E of primary photons incident on palladium. The total mass-attenuation coefficient (μ/ρ) results from the sum $(\tau/\rho) + (\sigma/\rho)$, the latter term from the sum of Rayleigh and Compton scattering $(\sigma/\rho)_R + (\sigma/\rho)_C$. Figure from Ref. [57], reproduced with permission from Center for X-Ray Optics and Advanced Light Source, Lawrence Berkeley National Laboratory, <http://xdb.lbl.gov>.

Compton scattering in the given energy range; the Rayleigh part is predominant for energies below 90 keV, the Compton part dominates for energies above 90 keV. Both effects are relatively minor compared to the photoelectric absorption. But for energies above 200 keV, the Compton effect becomes the decisive component of total attenuation. Similar conditions are valid for elements lighter or heavier than palladium. For light elements like carbon, the point of balance between Rayleigh and Compton scattering decreases to 10 keV; for heavy elements like lead, it increases to 150 keV [57].

It should be noted that the total mass-attenuation coefficient (μ/ρ) is mainly determined and equal to the photoelectric mass-absorption coefficient (τ/ρ) for lower photon energies (< 20 keV). For most elements ($Z > 14$) and energies between 5 and 20 keV, the quantities (μ/ρ) and (τ/ρ) differ by only about 0.01% up to 3%, relatively. In such cases, only one single set of data may be necessary for both quantities. For light elements like carbon and energies > 20 keV, however, the quantities (μ/ρ) and (τ/ρ) are different and have to be distinguished.

In practice, energy-dependent attenuation is used to alter the spectrum of an X-ray beam. For that purpose, a thin metal sheet called a selective attenuation filter can be employed. It can easily be inserted into a beam path in order to reduce a particular spectral peak or an entire energy band with respect to other peaks or spectral regions.

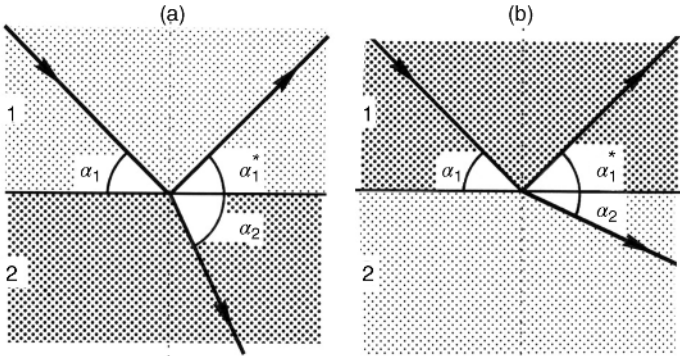


Figure 1.29. The incident, the reflected, and the refracted beam at the interface of media 1 and 2. On the left, medium 2 is optically denser than medium 1 ($n_2 > n_1$); on the right, it is vice versa ($n_1 > n_2$). The latter is usually the case for X-rays though it is exaggerated here. Figure from Ref. [8], reproduced with permission. Copyright © 1996, John Wiley and Sons.

1.5 DEFLECTION OF X-RAYS

In a homogeneous medium, the X-ray beam just behaves like a light beam and follows a straight path on which the photons travel. But if the beam hits the boundary surface of a second medium, the incident X-ray beam will be deflected from its original direction. It can even be split, that is, partly reflected into the first medium and partly refracted into the second medium.

1.5.1 Reflection and Refraction

In accord with Figure 1.29, the following rules are valid:

- The incident, the reflected, and the refracted beam span a plane that is normal to the boundary plane.
- The *glancing angles*² of the *incident* and the *reflected* beam are equal:

$$\alpha_1 = \alpha_1^* \quad (1.50)$$

- The *glancing angles* of the *incident* and the *refracted* beam follow Snell's law (also called Snellius' law):

$$v_2 \cos \alpha_1 = v_1 \cos \alpha_2 \quad (1.51)$$

² Glancing angles are considered in X-ray optics. They are complements of the angles of incidence conventionally used in light optics.

where v_1 and v_2 are the phase velocities of the beam in media 1 and 2, respectively. Phase velocity is the velocity at which the planes of constant phase, for example, crests or troughs, propagate within a medium. It is dependent on the wavelength, λ , and the medium itself. *In vacuo*, the phase velocity takes the value c_0 (the light velocity) independent of λ .

Division of Equation 1.51 by c_0 results in

$$n_1 \cos \alpha_1 = n_2 \cos \alpha_2 \quad (1.52)$$

where n_1 and n_2 are the absolute refractive indices of media 1 and 2, respectively, which are defined by

$$n_{1,2} = c_0/v_{1,2} \quad (1.53)$$

The refractive index is the fraction by which the phase velocity of the radiation is changed with respect to its vacuum value. For vacuum, the refractive index is 1.

The wavelength of a wave is changed by refraction and the photon energy is changed inversely to phase velocity and wavelength, though only a little bit. Division of Equation 1.51 by the frequency leads to

$$\lambda_2 \cos \alpha_1 = \lambda_1 \cos \alpha_2 \quad (1.54)$$

Two cases can be distinguished, as demonstrated in Figure 1.29. If $n_2 > n_1$, that is, if medium 2 is optically denser than medium 1, the refracted beam in medium 2 will be deflected *off* the boundary. If $n_2 < n_1$, that is, if medium 2 is optically thinner than medium 1, the refracted beam in medium 2 will be deflected *toward* the boundary.

The refractive index is the decisive quantity and can be derived from the so-called Lorentz theory assuming that the quasi-elastically bound electrons of the atoms are forced to oscillations by the primary radiation. As a result, the oscillating electrons radiate with a phase difference. By superposition of both radiations the primary one is altered in phase velocity. This alteration becomes apparent by a modified refractive index, deviating from the vacuum value $n_{\text{vac}} = 1$ by a small quantity δ .

If absorption cannot be neglected but has to be taken into account, the refractive index n has to be written as a complex quantity. Conventionally, n is defined by

$$n = 1 - \delta - i\beta \quad (1.55)$$

where i is the imaginary unit or the square root of -1 .³

³The refractive index n can be also defined by the conjugate complex quantity $1 - \delta + i\beta$.

The *imaginary* component β is a measure of the attenuation already treated in Section 1.4. It can be expressed by

$$\beta = \frac{\lambda}{4\pi} \left(\frac{\mu}{\rho} \right) \rho \quad (1.56)$$

The *real* part δ , called the *decrement*, measures the deviation of the *real* component $n' = 1 - \delta$ of the refractive index from unity. n' determines the phase velocity according to $v \approx c_0/n'$, which can even be greater than the light velocity.⁴

From theory it follows that δ can be written as [74]

$$\delta = \frac{N_A}{2\pi} r_{\text{el}} \frac{1}{A} [f_0 + f(\lambda)] \rho \lambda^2 \quad (1.57)$$

where N_A is Avogadro's number $= 6.022 \times 10^{23}$ atoms/mol, r_{el} is the classical electron radius $= \alpha_f \hbar c_0/E_0 = 2.818 \times 10^{-13}$ cm, A is the atomic mass of the respective element (in g/mol), ρ is the density (in g/cm³), and λ is the wavelength of the primary beam. f_0 is a quantity that for X-rays is equal to the atomic number Z of the particular element and $f(\lambda)$ is a correction term [75] that is only decisive at and above the absorption edges ($E \leq E_j$ or $\lambda \geq \lambda_j$) and is generally negative. Consequently, δ includes some constants of matter and moreover strongly depends on the wavelength. This dependence is known as dispersion and demonstrated in Figure 1.30 for the elements copper and gold.

For primary X-rays—shorter in wavelength than the absorption edges—the f values disappear and Equation 1.48 can be simplified by

$$\delta = \frac{N_A}{2\pi} r_{\text{el}} \frac{Z}{A} \rho \lambda^2 \quad (1.58)$$

The first factors can be combined to one single factor, which is a material constant:

$$C_m = \frac{N_A}{2\pi} r_{\text{el}} \frac{Z}{A} \rho \quad (1.58a)$$

In addition to Z , A , and ρ , this product is listed in Table 1.7 and represented in Figure 1.31 for pure elements. The values cover the range between $1 \times 10^{10}/\text{cm}^2$ for light elements, $3.137 \times 10^{10}/\text{cm}^2$ for silicon, and $25 \times 10^{10}/\text{cm}^2$ for heavy

⁴For X-rays with positive δ values, the phase velocity v exceeds the light velocity c_0 . Only the speed of particles with a rest mass above zero, that is, the velocity of signals, has to be smaller than the upper limit c_0 . The phase velocity, however, is not a velocity by which a real signal can be transmitted. Consequently, v can exceed c_0 .

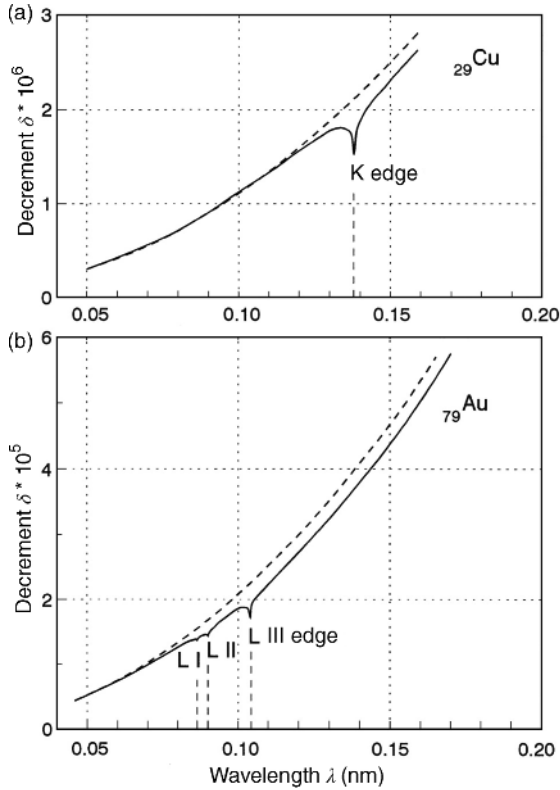


Figure 1.30. Dependence of the decrement δ on the wavelength λ for the elements (a) copper and (b) gold. The theory is based on forced oscillations of the atomic electrons—forced by the electromagnetic radiation of X-rays. At the “resonance” wavelengths or absorption edges, the decrement shows a strong variation. The asymptotic approximation for short wavelengths is represented by a dashed line. Data from Ref. [75], reproduced with permission from Forschungszentrum Jülich.

metals. The material constant contains (N_A/A) , which represents the reciprocal volume of a single atom. This dependency becomes apparent in the figure.

Equation 1.58 leads to the simple formula

$$\delta = C_m \lambda^2 \quad (1.59)$$

For given λ values of the X-ray region, the δ values can easily be calculated. Because these values are quite small (between 2×10^{-7} and 5×10^{-3}), the real part $1 - \delta$ of the refractive index deviates only slightly from unity (between 0.995 and 0.9999998). The minus sign in $1 - \delta$ reflects the fact that the bound electrons follow the excitant photons only slowly, that is, with phase *opposition*.

TABLE 1.7. Atomic Number, Atomic Mass, Density, and Material Constant of Pure Elements

At. No. Z	Symbol	Atomic Mass A (g/mol)	Density ρ (g/cm ³)	Constant C_m (10 ¹⁰ /cm ²)	At. No. Z	Symbol	Atomic Mass A (g/mol)	Density ρ (g/cm ³)	Constant C_m (10 ¹⁰ /cm ²)
3	Li	6.941	0.534	0.623	48	Cd	112.411	8.65	9.976
4	Be	9.0122	1.848	2.215	49	In	114.818	7.31	8.426
5	B	10.811	2.34	2.923	50	Sn	118.71	7.31	8.316
6	C	12.0107	2.1	2.833	51	Sb	121.76	6.691	7.569
7	N	14.0067	0.808	1.091	52	Te	127.6	6.24	6.868
8	O	15.9994	1.14	1.540	53	I	126.9045	4.93	5.561
9	F	18.9984	1.5	1.919	54	Xe	131.29	3.52	3.910
10	Ne	20.1797	1.207	1.615	55	Cs	132.9055	1.873	2.093
11	Na	22.9898	0.971	1.255	56	Ba	137.327	3.62	3.987
12	Mg	24.305	1.738	2.318	57	La	138.9055	6.145	6.811
13	Al	26.9815	2.6989	3.512	58	Ce	140.116	6.77	7.569
14	Si	28.0855	2.33	3.137	59	Pr	140.9077	6.773	7.660
15	P	30.9738	1.823	2.384	60	Nd	144.24	7.008	7.873
16	S	32.0653	2.07	2.790	61	Pm	144.91	7.264	8.259
17	Cl	35.4527	1.56	2.020	62	Sm	150.36	7.52	8.375
18	Ar	39.948	1.4	1.704	63	Eu	151.964	5.244	5.872
19	K	39.0983	0.862	1.131	64	Gd	157.25	7.901	8.685
20	Ca	40.078	1.55	2.089	65	Tb	158.9253	8.23	9.091
21	Sc	44.9559	2.989	3.771	66	Dy	162.5	8.551	9.380
22	Ti	47.867	4.54	5.636	67	Ho	164.9303	8.795	9.650
23	V	50.9415	6.11	7.451	68	Er	167.26	9.066	9.955
24	Cr	51.9961	7.19	8.963	69	Tm	168.93421	9.321	10.282
25	Mn	54.938	7.32	8.997	70	Yb	173.04	6.966	7.611
26	Fe	55.845	7.874	9.901	71	Lu	174.967	9.841	10.786
27	Co	58.9332	8.9	11.013	72	Hf	178.49	13.31	14.501

(continued)

TABLE 1.7. (Continued)

At. No. Z	Symbol	Atomic Mass A (g/mol)	Density ρ (g/cm^3)	Constant C_m ($10^{10}/\text{cm}^2$)	At. No. Z	Symbol	Atomic Mass A (g/mol)	Density ρ (g/cm^3)	Constant C_m ($10^{10}/\text{cm}^2$)
28	Ni	58.6934	8.902	11.470	73	Ta	180.9479	16.654	18.146
29	Cu	63.546	8.96	11.044	74	W	183.84	19.3	20.982
30	Zn	65.39	7.133	8.839	75	Re	186.207	21.02	22.867
31	Ga	69.723	5.904	7.090	76	Os	190.23	22.57	24.354
32	Ge	72.61	5.323	6.336	77	Ir	192.217	22.42	24.257
33	As	74.9216	5.73	6.817	78	Pt	195.078	21.45	23.164
34	Se	78.96	4.79	5.571	79	Au	196.9665	19.31	20.918
35	Br	79.904	3.12	3.691	80	Hg	200.59	13.546	14.591
36	Kr	83.801	2.16	2.506	81	Tl	204.3833	11.85	12.684
37	Rb	85.4678	1.532	1.791	82	Pb	207.2	11.35	12.132
38	Sr	87.62	2.54	2.975	83	Bi	208.98	9.747	10.456
39	Y	88.9059	4.469	5.295	84	Po	208.98	9.32	10.118
40	Zr	91.224	6.506	7.705	85	At	209.99	—	10.149
41	Nb	92.9064	8.57	10.215	86	Rn	222.02	9.73	10.179
42	Mo	95.9108	10.22	12.087	87	Fr	223.02	—	10.704
43	Tc	97.907	11.5	13.641	88	Ra	226.03	—	11.229
44	Ru	101.07	12.41	14.592	89	Ac	227.03	—	11.754
45	Rh	102.9255	12.41	14.654	90	Th	232.038	11.72	12.278
46	Pd	106.4252	12.02	14.032	91	Pa	231.036	15.37	16.351
47	Ag	107.8682	10.49	12.345	92	U	238.029	19.16	20.001

Density of solids and liquids were determined at 20 °C and given in g/cm^3 ; density of gaseous elements were determined at the boiling point for the liquids. Source: From Ref. [57]; courtesy of Center for X-Ray Optics and Advanced Light Source, Lawrence Berkeley National Laboratory.

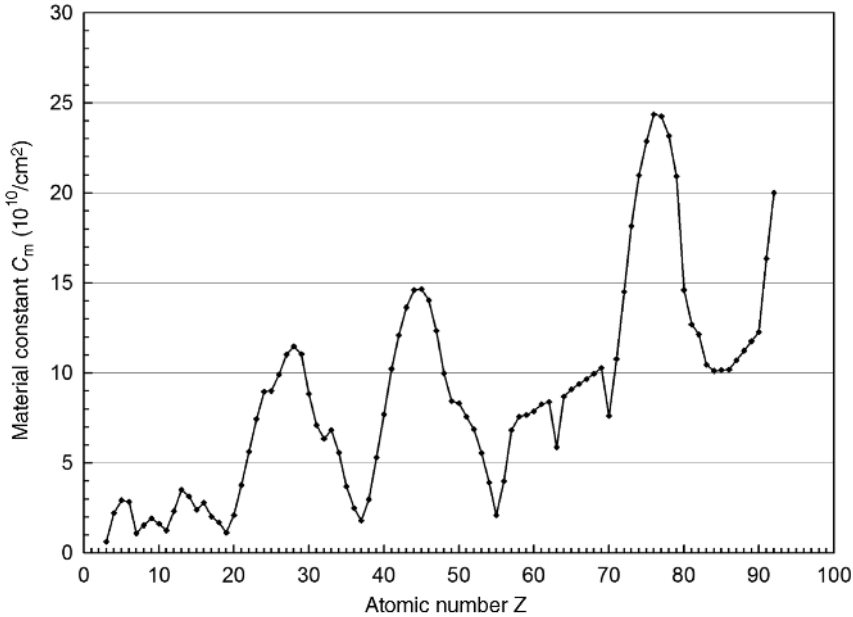


Figure 1.31. Material constant C_m defined by Equation 1.58a and calculated for different pure elements with atomic number Z . The maxima at $Z=14, 28, 45,$ and 77 reflect a small volume of the respective atoms while the minima at $Z=11, 19, 37, 55,$ and 85 occur for relatively large atoms (alkali metals). The quantity is important for the calculation of the refractive index and the critical angle of total reflection. Data from <http://xdb.lbl.gov>; reproduced with permission from Center for X-Ray Optics and Advanced Light Source, Lawrence Berkeley National Laboratory.

The small quantity of δ is due to the small amplitude of the electrons' oscillations. Because of the high photon frequencies corresponding to the short wavelengths of X-rays, only small amplitudes can occur.

The quantity β is even smaller than δ . Table 1.8 lists values of δ and β for some compounds and pure elements, calculated for Mo- $K\alpha$ radiation. For compounds, solutions, or mixtures, δ and β have to be calculated according to the additive law already applied in Equation 1.41:

$$\delta_{\text{total}} = \sum c_i \delta_i \quad (1.60)$$

$$\beta_{\text{total}} = \sum c_i \beta_i \quad (1.61)$$

Again, the c_i terms are the different mass fractions of the individual elements i with respective values δ_i and β_i .

1.5.2 Diffraction and Bragg's Law

The phenomenon of a so-called diffraction occurs when a wave hits an obstacle. A parallel wave front hitting a small obstacle or opening deviates from its

TABLE 1.8. The Real Part δ and the Imaginary Part β of the Refractive Index n Calculated for Mo-K α X-rays with $\lambda = 0.071 \text{ nm}^a$

Medium	$\rho \text{ (g/cm}^3\text{)}$	$\delta \text{ (}10^{-6}\text{)}$	$\beta \text{ (}10^{-8}\text{)}$
Plexiglas	1.16	0.9	0.055
Glassy carbon	1.41	1.0	0.049
Boron nitride	2.29	1.5	0.090
Quartz glass	2.20	1.5	0.46
Aluminum	2.70	1.8	0.79
Silicon	2.33	1.6	0.84
Cobalt	8.92	5.6	19.8
Nickel	8.91	5.8	21.9
Copper	8.94	5.6	24.1
Germanium	5.32	3.2	18.7
Gallium arsenide	5.31	3.2	18.7
Tantalum	16.6	9.1	87.5
Platinum	21.45	11.7	138.2
Gold	19.3	10.5	129.5

^aThe various media with density ρ are listed in order of increasing (mean) atomic number.

Source: From Ref. [8], reproduced with permission. Copyright © 1996, John Wiley and Sons.

original straightforward direction, bends, and spreads into the geometric shadow. Respective patterns have been observed for different waves, including visible light already in the seventeenth century. When several closely spaced obstacles or openings are encountered, the original primary wave will induce several original secondary waves after Huygens' principle. These waves will interfere with each other and show intensity maxima by constructive interference and show minimum or even zero intensity by destructive interference.

Around the turn of the nineteenth century, it was assumed that most solids are composed of crystals with a regular periodic arrangement of atoms. These atoms are fixed in a three-dimensional lattice with various two-dimensional lattice planes. Each set of planes has a spacing d_{hkl} , where (h, k, l) are called Miller indices. Values for spacing and X-ray wavelengths are of the same order of magnitude (between 0.05 and 0.5 nm), which is a prerequisite for diffraction to occur.

In 1912, Max von Laue, Friedrich, and Knipping demonstrated how X-rays were diffracted by crystals. They irradiated a single inorganic crystal (copper sulfate pentahydrate) with a fine, millimeter-wide X-ray beam and discovered several symmetrical points of deflection behind the crystal. Difficult calculations were needed to explain the diffraction by a three-dimensional array of atoms. The Braggs, however, used a narrow line-focused X-ray beam. As already demonstrated in Figure 1.2, it was diffracted at a polished plate of an inorganic crystal (e.g., NaCl, ZnS, and diamond). The X-ray beam was scattered by the atoms of the rotating crystal in a goniometer at certain angles

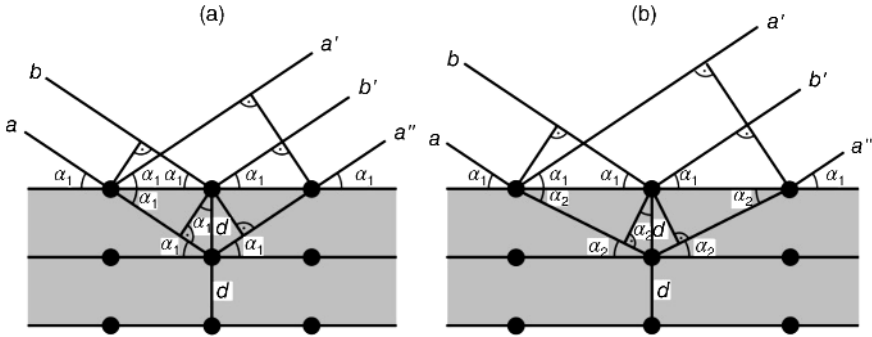


Figure 1.32. Bragg's reflection of two parallel X-ray beams a and b at parallel lattice planes of a crystal filled with scattering atoms. Neighboring planes have a constant distance d . (a) Without refraction of the incoming beam a . (b) With its refraction at the upmost lattice plane. The beams aa' and bb' are reflected at the upmost plane, the beam aa'' is refracted at the upmost plane and reflected at the next deeper plane. The geometric path difference is the length of the small sides of the kites within both figures given by $2d\sin\alpha_1$ (Figure 1.32a) or $2d\sin\alpha_2$ (Figure 1.32b). For maximum reflectivity, this difference has to be an integer multiple of the respective wavelength λ_1 of the incoming beam (Figure 1.32a) or λ_2 of the refracted and penetrating beam (Figure 1.32b).

α_1 , blackening a photographic film under angles $2\alpha_1$. Calculations became easy since the diffraction could be interpreted as reflections of X-rays at crystal lattice planes followed by their constructive interference at certain angles α_1 .

The derivation of Bragg's law is demonstrated in Figure 1.32. A wave between two parallel beams coming from vacuum a and b hits a crystal with parallel lattice planes under an incident angle α_1 . These planes are filled with atoms, the inner electrons of which can elastically scatter the incoming wave (Rayleigh scattering). The wave ab is reflected at the upmost layer under the angle α_1 leading to the wave $a'b'$. On the left of this figure, the incoming beam a also penetrates the upmost plane without refraction, is reflected at the next deeper plane, and returns to vacuum under the angle α_1 . On the right, beam a is additionally refracted and enters the crystal at a glancing angle α_2 , which for X-rays is somewhat smaller than α_1 . The refracted beam is reflected at the next deeper plane leading to the beam a'' that leaves the crystal at the glancing angle α_1 . The path difference of the neighboring reflected beams aa' and bb' is zero, but the path difference of these two beams with the refracted and reflected beam aa'' is either $2d\sin\alpha_1$ (Figure 1.32a) or $2d\sin\alpha_2$ (Figure 1.32b). If this difference is an integer multiple of wavelength λ_1 (Figure 1.32a) or λ_2 (Figure 1.32b), both beams are in phase and we have constructive interference. All lattice planes cooperate in the same direction and we get maximum intensity of all reflected and refracted beams. If the difference is an odd multiple of half the wavelength we have destructive interference with minimum intensity or extinction.

Originally, Bragg's law was derived for X-rays when the refraction of the incoming beam by the crystal could be neglected (Figure 1.32a); that means $\alpha_1 = \alpha_2$ and $\lambda_1 = \lambda_2$. The condition for maximum reflectivity is given by

$$2d \sin \alpha_1 = m\lambda_1 \quad (1.62)$$

where m is a positive integer (1, 2, 3 . . .) also called order of reflection. If the refraction is taken into account we get a similar relation (Figure 1.32b):

$$2d \sin \alpha_2 = m\lambda_2 \quad (1.63)$$

where λ_2 and α_2 in the crystal medium can be related to λ_1 and α_1 in vacuum according to Snell's law of Equation 1.54. As already mentioned by Compton [7], Bragg's law in Equation 1.62 has to be corrected by a factor that depends on the decrement δ defined in Section 1.5.1:

$$2d \sin \alpha_1 \cdot (1 - \delta/\sin^2 \alpha_1) = m\lambda_1 \quad (1.64)$$

For X-rays with δ values smaller than 10^{-5} and angles above 1° , the correction factor in brackets is of the order of 0.99.

The diffraction of X-rays at crystals together with Bragg's law is the basis of wavelength-dispersive X-ray spectrometry when d is known and λ_1 has to be determined (see Chapter 3.7). On the other hand, it is the prerequisite for X-ray diffractometry if—conversely— λ_1 is known and d has to be measured, for example, in crystallography.

Because of experimental difficulties, further diffraction patterns for X-rays were observed not until 1929. X-rays with a wavelength of 0.08 nm were transmitted through a single fine slit with a width of 5.5 μm and showed a pattern with several lines in the shadow region, to the left and to the right of the passing beam and parallel to it [1]. Even later, ruled gratings were developed by Siegbahn and used for diffraction of X-rays at grazing incidence. By this means, X-ray wavelengths could be determined directly and very precisely. Together with Bragg's law, the spacing of crystal lattice planes could be measured to yield a precise value of Avogadro's number that may ultimately lead to the definition of the kilogram in terms of atomic constants.

1.5.3 Total External Reflection

For X-rays, any medium is optically less dense than vacuum ($n' < n_{\text{vac}} = 1$) and any solid is optically less dense than air ($n' < n'_{\text{air}} \approx 1$), which is in contrast to visible light. This results in a refracted beam that is deflected toward the boundary plane (Figure 1.32b). For a better understanding, the refraction is exaggerated here. Since δ is very small for X-rays, the refraction is very weak.

If the respective glancing angle α_2 of the refractive beam becomes zero, the refracted beam will emerge tangentially to the boundary surface. Consequently, there is a minimum critical angle $\alpha_1 = \alpha_{\text{crit}}$ for which refraction is just possible. According to Equation 1.52, this angle of incidence is determined by

$$\cos \alpha_{\text{crit}} = n_2 \quad (1.65)$$

For angles α_1 even lower than α_{crit} , Equation 1.52 gives no real value for the refraction angle α_2 since the cosine cannot be > 1 . In this case, no beam enters the second medium, but the boundary, like an ideal mirror, completely reflects the incident beam back into the first medium, that is, vacuum or air. This phenomenon is called “total *external* reflection.” In contrast to X-rays, visible light can undergo “total *internal* reflection” when the light comes from a solid medium below a critical angle. It does not enter the adjacent vacuum or air as the second medium, but is totally reflected back into this first medium.

The critical angle of total reflection can easily be calculated from Equation 1.65. Since α_{crit} is small, its cosine can be approximated by

$$\cos \alpha_{\text{crit}} \approx 1 - \frac{\alpha_{\text{crit}}^2}{2} \quad (1.66)$$

The combination with Equation 1.55 leads to the simple relation

$$\alpha_{\text{crit}} \approx \sqrt{2\delta} \quad (1.67)$$

Insertion of Equation 1.58 gives the approximation

$$\alpha_{\text{crit}} \approx \frac{1.651}{E} \sqrt{\frac{Z}{A}} \rho \quad (1.68)$$

where E has to be given in keV and ρ in g/cm^3 in order to get α_{crit} in degrees. This formula may be converted into

$$\alpha_{\text{crit}} \approx \frac{10^{-5}}{E} \sqrt{C_m} \quad (1.69)$$

As already mentioned for Equation 1.58, this approximation is exactly valid for photon energies above the decisive absorption edges of the material. Table 1.9 gives values for different media and photon energies frequently used for excitation: 8.4 keV is the energy of W- $L\alpha$ photons, 17.44 keV is the energy of Mo- $K\alpha$ photons, and 35 keV may represent the photon energy of the hump appearing in a continuous spectrum of an X-ray tube. All values of α_{crit} lie between 0.04° and 0.6° . For all other combinations of medium and photon energy, the critical angle can simply be calculated after Equation 1.69 and by use of Table 1.7.

TABLE 1.9. Critical Angle α_{crit} of Total Reflection, Calculated for Various Media and X-rays of Different Photon Energies

Medium	α_{crit} at Photon Energy of		
	8.4 keV (degree)	17.44 keV (degree)	35 keV (degree)
Plexiglas	0.157	0.076	0.038
Glassy carbon	0.165	0.080	0.040
Boron nitride	0.21	0.10	0.050
Quartz glass	0.21	0.10	0.050
Aluminum	0.22	0.11	0.054
Silicon	0.21	0.10	0.051
Cobalt	0.40	0.19	0.095
Nickel	0.41	0.20	0.097
Copper	0.40	0.19	0.095
Germanium	0.30	0.15	0.072
Gallium arsenide	0.30	0.15	0.072
Tantalum	0.51	0.25	0.122
Platinum	0.58	0.28	0.138
Gold	0.55	0.26	0.131

Source: From Ref. [8], reproduced with permission. Copyright © 1996, John Wiley and Sons.

In the range of total reflection, calculations have to be carried out on complex refraction angles α_2 with a real and an imaginary part. Nevertheless, for our purposes, it is possible to make this task a lot easier, as simple approximations can be applied for the small glancing angles considered in X-ray optics.

In accord with Figure 1.32 b, X-rays are assumed to run through a vacuum and then to strike a medium at an angle α_1 . In this case, the angle α_2 of the refracted beam has to be considered complex. Assuming Snell's law (1.52) and neglecting higher powers of small quantities we get

$$\alpha_2 \approx \sqrt{\alpha_1^2 - 2\delta - 2i\beta} \quad (1.70)$$

where δ and β belong to the complex refractive index n of the medium. The real and imaginary components of this angle, α_2 and α_2' , respectively, can be written as (see, e.g., Refs [75,76])

$$\alpha_2^2 = \frac{1}{2} \left[\sqrt{(\alpha_1^2 - 2\delta)^2 + (2\beta)^2} + (\alpha_1^2 - 2\delta) \right] \quad (1.71)$$

$$\alpha_2'^2 = \frac{1}{2} \left[\sqrt{(\alpha_1^2 - 2\delta)^2 + (2\beta)^2} - (\alpha_1^2 - 2\delta) \right] \quad (1.72)$$

Both components are represented in Figure 1.33 for Mo-K α X-rays striking a flat silicon substrate. The real component, α_2' , is dominant in the range above the critical angle α_{crit} and is asymptotically equal to α_1 for large angles. The

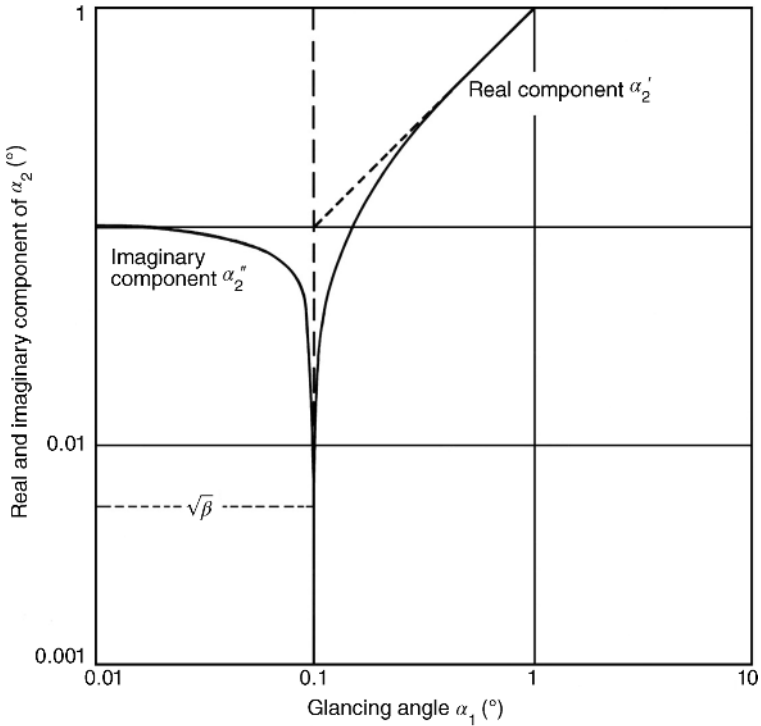


Figure 1.33. Double logarithmic plot of the real and imaginary component determining the angle α_2 of the refracted X-ray beam in dependence on the glancing angle α_1 of the incident beam. Calculation for Mo-K α X-rays striking a flat silicon substrate above and below the critical angle of total reflection that amounts to 0.1°. Figure from Ref. [8], reproduced with permission. Copyright © 1996, John Wiley and Sons.

imaginary component, α_2'' , is decisive for angles below α_{crit} and is asymptotically equal to α_{crit} for small angles. Both components become equal at the critical angle and amount to $\sqrt{\beta}$, which is extremely small. Moreover, the product of both components always equals β independent of the given glancing angle of incidence:

$$\alpha_2' \cdot \alpha_2'' = \beta \tag{1.73}$$

This relationship can easily be verified by multiplication of Equations 1.71 and 1.72 and extraction of the roots. It is important for subsequent calculations in Section 2.4.

For total reflection, two important quantities are characteristic:

- The reflectivity R , which is increased to 100% below the critical angle.
- The penetration depth z_n , which is reduced to a few nanometers in this case.

Both quantities can be calculated from the theory of a harmonic and plane electromagnetic wave, as discussed in Sections 1.5.3.1 and 1.5.3.2.

1.5.3.1 Reflectivity

The reflectivity is defined by the intensity ratio of the reflected beam and the incident beam and can be derived from the Fresnel formulas. These well-known formulas connect the vectors of the electromagnetic field of the reflected and the transmitted beam with those of the incident beam [77]. For the grazing incidence considered here, the amplitudes E_1^i , E_1^r , and E_2^t of the electric field vectors are expressed by the simple formulas

$$\begin{aligned}\frac{E_1^r}{E_1^i} &= \frac{\alpha_1 - \alpha_2}{\alpha_1 + \alpha_2} \\ \frac{E_2^t}{E_1^i} &= \frac{2\alpha_1}{\alpha_1 + \alpha_2}\end{aligned}\tag{1.74}$$

These formulas are valid independent of the polarization of the incident beam because of the assumed small angles α_1 and α_2 . The reflectivity and transmissivity follow from these formulas after the absolute magnitude is squared.

The reflectivity R is given by

$$R = \left| \frac{\alpha_1 - \alpha_2}{\alpha_1 + \alpha_2} \right|^2\tag{1.75}$$

With the help of the components α_2' and α_2'' of the complex angle α_2 , the reflectivity can be calculated:

$$R = \frac{(\alpha_1 - \alpha_2')^2 + \alpha_2''^2}{(\alpha_1 + \alpha_2')^2 + \alpha_2''^2}\tag{1.76}$$

Three highly useful approximations result:

$$\begin{aligned}\alpha_1 \ll \alpha_{\text{crit}}: \quad R &\cong 1 - \sqrt{\frac{2\beta}{\delta}} \frac{\beta}{\delta} \alpha_1 \\ \alpha_1 = \alpha_{\text{crit}}: \quad R &\approx \frac{\delta + \beta - \sqrt{(2\beta\delta)}}{\delta + \beta + \sqrt{(2\beta\delta)}} \\ \alpha_1 \gg \alpha_{\text{crit}}: \quad R &\cong \frac{\delta^2}{4\alpha_1^4}\end{aligned}\tag{1.77}$$

The dependence of the reflectivity on the glancing angle is demonstrated in Figure 1.34. The effect of total reflection is shown for three different elements.

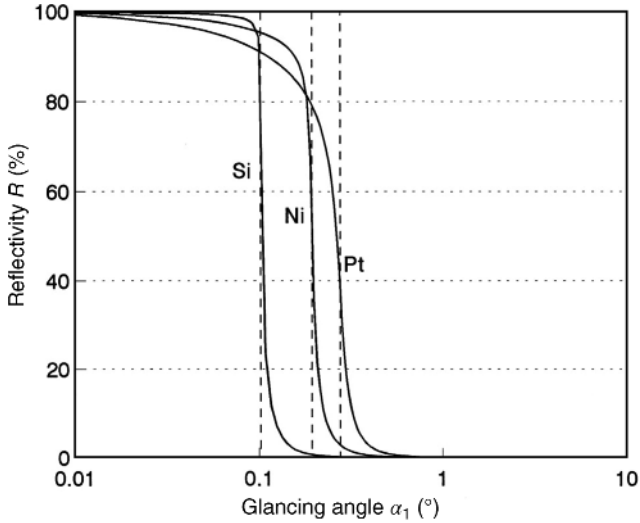


Figure 1.34. Reflectivity of three different media dependent on the glancing angle of X-rays. The curves were calculated for X-rays of Mo-K α . Reflection below a critical angle α_{crit} is called *total reflection*. These angles are determined by the point of inflection of the curves and are marked by dashed vertical lines. Figure from Ref. [8], reproduced with permission. Copyright © 1996, John Wiley and Sons.

For glancing angles of 1° or more, the reflectivity is below 0.1%, independent of absorption, and can be neglected generally. Around the critical angle, the reflectivity rises to high values. However, the rise to 100% is not steplike but more or less gradual, dependent on the absorption or attenuation quantity β . The critical angle determines the point of inflection of the curves. For a less absorbing medium like silicon, the reflectivity shows the most distinct transition. For this reason silicon or quartz glass and even Plexiglas are used as sample carriers for TXRF.

The curves of Figure 1.34 were calculated for X-rays of Mo-K α with photon energy of 17.44 keV. For higher energies, the α_{crit} values are decreased according to the $1.65/E$ term in Equation 1.68 and consequently the curves are shifted to the left. For lower energies, they are shifted to the right. Table 1.10 lists the corresponding reflectivity values calculated by Equation 1.77.

1.5.3.2 Penetration Depth

The penetration depth is defined by that depth of a homogeneous medium a beam can penetrate while its *intensity* is reduced to $1/e$, or 37% of its initial value. This depth z_n , which is normal to the boundary of the medium, follows the equation

$$z_n \approx \frac{\lambda}{4\pi} \frac{1}{\alpha_2''} \quad (1.78)$$

TABLE 1.10. Reflectivity R_{crit} of Various Media at the Critical Angle of Total Reflection, Calculated for X-rays of Different Photon Energies

Medium	R_{crit} at Photon Energy		
	8.4 keV (%)	of: 17.44 keV (%)	35 keV (%)
Plexiglas	87.9	93.2	94.8
Glassy carbon	88.4	93.9	95.0
Boron nitride	87.6	93.3	94.6
Quartz glass	73.4	85.5	91.4
Aluminum	69.7	82.9	90.3
Silicon	67.3	81.5	89.5
Cobalt	37.4	59.1	75.2
Nickel	37.0	58.1	74.9
Copper	66.9	56.1	82.7
Germanium	62.3	51.2	69.7
Gallium arsenide	62.4	51.1	69.5
Tantalum	49.3	42.9	63.4
Platinum	45.3	39.4	60.2
Gold	44.8	38.7	59.5

Source: From Ref. [8], reproduced with permission. Copyright © 1996, John Wiley and Sons.

Again three approximate values can be given:

$$\begin{aligned}
 \alpha_1 \ll \alpha_{\text{crit}}: \quad z_n &\approx \frac{\lambda}{4\pi} \frac{1}{\sqrt{2\delta}} \\
 \alpha_1 = \alpha_{\text{crit}}: \quad z_n &\approx \frac{\lambda}{4\pi} \frac{1}{\sqrt{\beta}} \\
 \alpha_1 \gg \alpha_{\text{crit}}: \quad z_n &\approx \frac{\lambda}{4\pi} \frac{\alpha_1}{\beta}
 \end{aligned} \tag{1.79}$$

For $\alpha \geq \alpha_{\text{crit}}$, the penetration depth is dependent on β , which is proportional to the mass-absorption coefficient of the medium. For $\alpha < \alpha_{\text{crit}}$, however, δ becomes the decisive quantity, which is mainly determined by atomic constants of the medium.

Figure 1.35 shows a double-logarithmic presentation of the penetration depth dependent on the glancing angle for the three elements already considered in Figure 1.34. For angles above and down to 0.5° , the penetration depth linearly decreases with the glancing angle and the depth values are of the order of $0.1\text{--}10\ \mu\text{m}$. At the critical angle, the penetration depth drastically decreases especially for nonabsorbing media like silicon. Below this critical angle, the penetration depth reaches a constant level of only a few nanometers and the beam is called “evanescent.” For silicon, the three z_n values of Equation 1.79 come to $3.2\ \text{nm}$, $62\ \text{nm}$, and $1.2\ \mu\text{m} \times (\alpha/\alpha_{\text{crit}})$.

Of course, the effect of total reflection only appears when the medium is flat and smooth. For a rough surface, total reflection disappears. The penetration

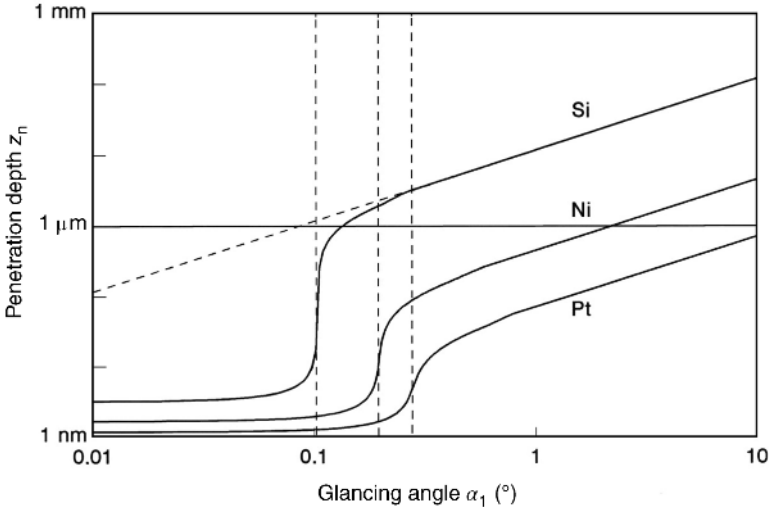


Figure 1.35. Penetration depth of X-rays hitting three different media at a variable glancing angle. The curves were calculated for X-rays of Mo-K α with a photon energy of 17.44 keV. The critical angles are marked by dashed vertical lines. The dashed oblique straight line represents the penetration depth in a roughened silicon surface for which total reflection disappears. Figure from Ref. [8], reproduced with permission. Copyright © 1996, John Wiley and Sons.

depth linearly decreases with the glancing angle even below the critical angle, as is demonstrated in Figure 1.35 for silicon.

The curves of Figure 1.35 were calculated for the photon energy of the chosen Mo-K α radiation. The influence of the different photon energies on the penetration depth is shown in Figure 1.36—here for silicon. The points of inflection shift to lower critical angles with increasing photon energy. Furthermore, the curves are stretched to higher depth values for normal reflection while the depth values for total reflection remain constant at

$$z_0 \cong 3.424 \sqrt{\frac{A}{Z} \frac{1}{\rho}} \quad (1.80)$$

This minimum is a material constant that is only dependent on the quantity C_m but is independent of the photon energy and is listed in Table 1.11 for various media. This table also gives critical penetration depths calculated for α_{crit} and three different photon energies according to Equation 1.79.

In comparison to the penetration depth, a further quantity is important—the information depth. It is the depth of a sample from which secondary radiation emerges and reaches the detector for X-ray fluorescence analysis. This information depth is always smaller than the penetration depth. For high-energy peaks (energy of the emitted radiation is only a little smaller than the photon energy of the primary radiation used for excitation) it is of the order of the

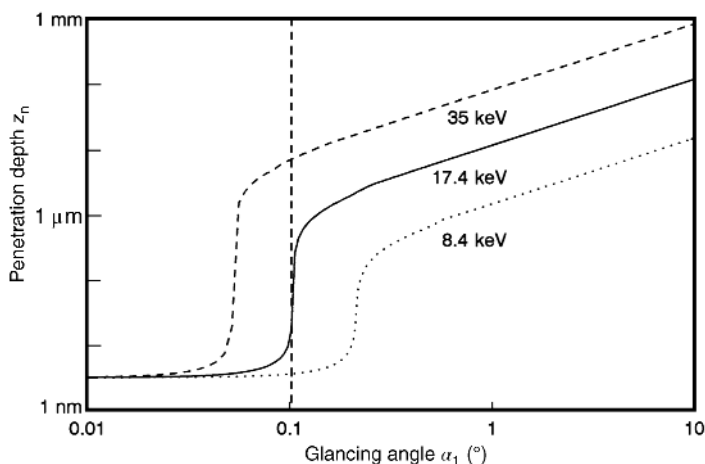


Figure 1.36. Penetration depth of X-rays striking on silicon at a variable glancing angle. The curves were calculated for three different photon energies. The dashed vertical line identifies the respective critical angle for photons with $E = 17.4$ keV. Figure from Ref. [8], reproduced with permission. Copyright © 1996, John Wiley and Sons.

TABLE 1.11. Minimum Penetration Depth z_0 and Critical Penetration Depth z_{crit} of Various Media, Calculated for X-rays of Different Photon Energies

Medium	Minimum z_0 (nm)	8.4 keV (nm)	z_{crit} at Photon Energy of: 17.44 keV (nm)	35 keV (nm)
Plexiglas	4.3	132	241	319
Glassy carbon	4.1	130	255	311
Boron nitride	3.2	97	188	238
Quartz glass	3.2	42	83	146
Aluminum	3.0	33	64	116
Silicon	3.2	32	62	115
Cobalt	1.7	6.6	12.7	24
Nickel	1.7	6.4	12.1	23
Copper	1.7	16.8	11.5	22
Germanium	2.2	18.8	13.1	25
Gallium arsenide	2.2	18.8	13.0	24
Tantalum	1.3	7.3	6.0	11.4
Platinum	1.2	5.8	4.8	9.1
Gold	1.2	6.0	5.0	9.4

Source: From Ref. [8], reproduced with permission. Copyright © 1996, John Wiley and Sons.

penetration depth. However, for low-energy peaks (energy of emitted photons is much smaller than that of primary photons) the information depth can be 10 times smaller or even less compared to the penetration depth.

1.5.4 Refraction and Dispersion

In light optics, the phenomenon of dispersion can be demonstrated by a triangular prism or by a plane parallel plate.⁵ A rainbow is the most familiar example where the moisture in the atmosphere represents a lot of tiny drops. By refraction, the white polychromatic light beam splits into its component colors geometrically and leads to a “spectrum.” The red color is always bent least and the violet color is bent most. The phenomenon is based on the fact that the refractive index of a substance depends on the wavelength or energy of the photons used to measure it. The refractive index is about 1.3 for water, about 1.5 for different glasses, and about 2.4 for diamond at $\lambda = 589 \text{ nm}$ (Na yellow).

The phenomena of refraction and dispersion also occur for X-rays with a subtle distinction; the refractive index is usually a little bit smaller than 1 (about 0.995 for 1 keV photons in platinum, up to 0.9999998 for 40 keV photons in Plexiglas). The effect is demonstrated by a polychromatic X-ray beam coming from vacuum or air and refracted at a plane-parallel plate, for example, a rectangular piece of a wafer, as illustrated in Figure 1.37. This incident beam may hit the plate at an incident glancing angle α_1 is refracted at the upper plane, and split into beams of particular wavelengths or photon energies at different exit angles α_2 . All these X-ray beams are deflected in the direction of the plate surface (in contrast to visible light). The larger the wavelength of the X-radiation, that is, the smaller the photon energy E_2 the smaller the corresponding refraction angle. All the refracted beams are refracted a second time at the bottom plane and leave the plate in parallel to each other but with a different distance in the x direction. The exit beam in total is parallel to the incident primary beam but split into parts of different photon energies and shifted to the right.

Investigations go back to an early paper of Yoneda in 1963 [79] who investigated the refraction and reflection of an X-ray beam of a Mo tube at a plane-parallel plate of silicon. He observed an anomalous surface reflection (ASR) near the critical angle of total reflection (see also Ref. [80]). A photograph shows several lines: the totally reflected line, an ASR band, an artificial center line between totally reflected and directly passing beam, the $K\alpha$ and $K\beta$ lines of Mo, and the directly passing beam (without plate).

For a given glancing angle of the incident beam, the glancing angle of the exit beam is determined by Snell’s law according to Equation 1.52. For glancing angles above the critical angle of total reflection, the wavelength of the refracted beam increases only slightly and α_2 is somewhat smaller than α_1 as

⁵ A plane-parallel plate can be defined as a rectangular parallelepiped or a rectangular prism.

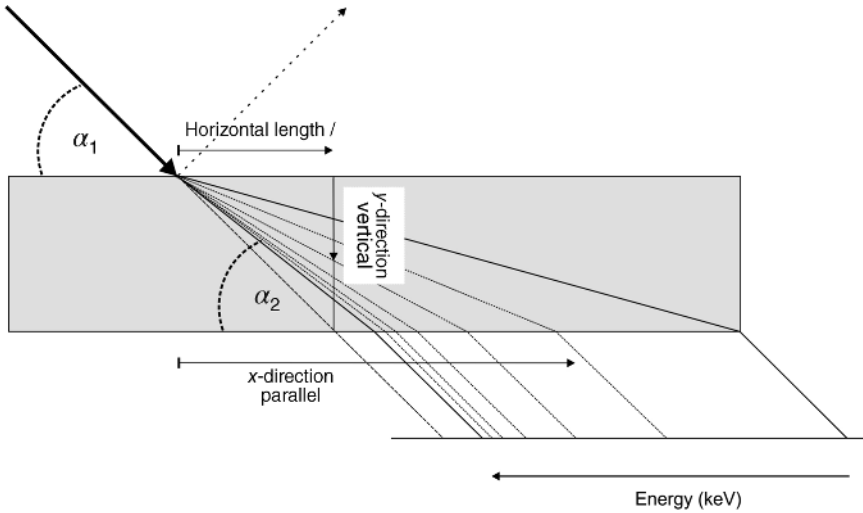


Figure 1.37. Dispersion of X-rays by refraction at a plane-parallel plate or a “rectangular prism,” respectively. The incident polychromatic beam with several different photon energies strikes a silicon wafer plate at a fixed glancing angle α_1 . The beam is reflected at the same angle with a small intensity of only about 1% in the range of 0.1° to 0.2° as is indicated by a dashed line. In addition, the beam is refracted under exit angles α_2 dependent on respective photon energies, E_2 , with an intensity of about 99% (after Ref. [78]). In a horizontal distance x dependent on α_2 and E_2 , all the refracted beams leave the silicon plate at the original α_1 . The exit beam in total is parallel to the incident primary beam but is shifted to the right in dependency of the energy E_2 . If the wafer has a thickness of 0.5 mm the parallel shift is of the order of several 10 cm. A vertical shift of about some $10\ \mu\text{m}$ can be observed if the wafer is cut in a distance of 10 mm.

demonstrated in Figure 1.32b.⁶ For glancing angles below the critical angle of total reflection $\alpha_1 < \alpha_{\text{crit}}$, there is no refracted beam but only the reflected beam with an intensity of nearly 100%.

The glancing angle of the refracted exit beam α_2 for a given incident glancing angle α_1 can be calculated in accord with Snell’s law. We find the approximation for the refractive index of a substance [78,81,82]:

$$n_2 = 1 - \left(\frac{\alpha_1^2}{2} - \frac{\alpha_2^2}{2} \right) \quad (1.81)$$

Comparison with Equation 1.67 leads to

$$\lambda_2 = \lambda_{\text{cut}} \frac{\sqrt{\alpha_1^2 - \alpha_2^2}}{\alpha_{\text{crit}}} \quad (1.82)$$

⁶The wavelength of the refracted beam is increased negligibly by $1/n_2$; that is, by a factor smaller than 1.0005 for silicon or quartz glass.

where λ_{cut} is the longest wavelength of an X-ray beam that can be refracted at the given incident angle. A beam with a wavelength that is still longer than λ_{cut} will not be refracted but totally reflected. For X-rays, α_2 is somewhat smaller than α_1 and consequently the radicand is always positive.

Equation 1.82 can be transformed for photon energies of the refracted beam:

$$E_2 = E_{\text{cut}} \frac{\alpha_{\text{crit}}}{\sqrt{\alpha_1^2 - \alpha_2^2}} \quad (1.83)$$

where E_{cut} is the cutoff energy, which is the smallest possible photon energy of a beam that can be refracted; a beam with an even smaller photon energy is totally reflected. The product of E_{cut} and α_{crit} is constant for a specific material. It is equal to $hc_0 \cdot \sqrt{2C_m}$ and amounts to 1.778 for a silicon wafer if the energy is given in keV and the angle is entered in degrees. The photon energy of the exit beam is demonstrated in Figure 1.38 in dependence of the exit angle and four fixed incident angles. The range of possible exit angles is between 0° and α_1 and the respective range of photon energies is between E_{crit} and ∞ . In all cases, the photon energy of the incident beam E_1 is only a little bit higher than that of the exit beam E_2 .

Hayashi *et al.* investigated the refraction of X-rays in silicon at grazing incidence [78]. The authors turned a polychromatic beam of a Mo tube on a Si

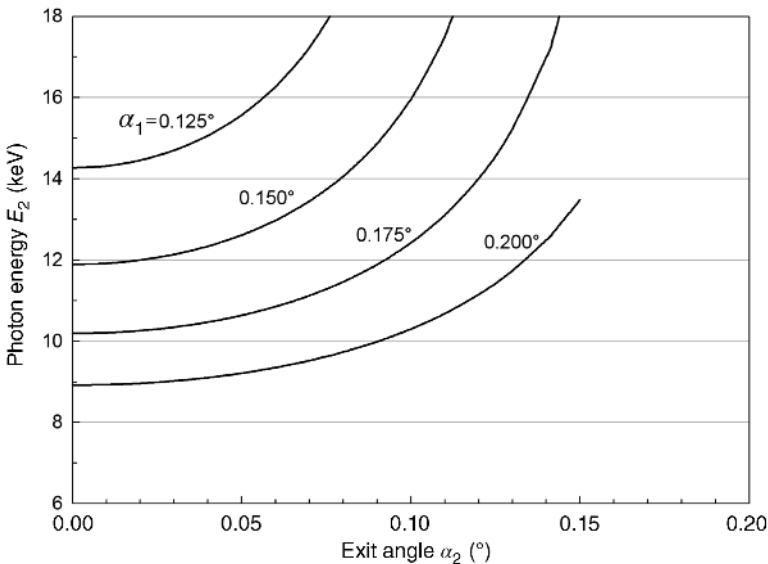


Figure 1.38. Energy of photons *in* the refracted beam dependent on the respective exit angle. It is provided that the incident beam strikes a silicon wafer at a fixed glancing angle of 0.125° , 0.150° , 0.175° , and 0.200° .

wafer under a small angle $\alpha_1 = 0.124^\circ$ and verified three single refracted peaks at angles of 0.02° , 0.04° , and 0.06° with an energy of 14.5, 15.1, and 16.4 keV, respectively, in accord with Equation 1.83. The width of these peaks was about 1 keV. Furthermore, a thin organic film of $n\text{-C}_{33}\text{H}_{68}$ was deposited on the Si carrier and the experiment repeated with $\alpha_1 = 0.095^\circ$. Again a refracted peak was found depending on α_2 with energies between 18.4–20.6 keV, but moreover a strong peak at 16.2 keV was recognized independent of α_2 . The relationships were proved true by Ebel *et al.* [81–83] in accord with Equation 1.83. Moreover, the additional peak could be explained by the organic overlay acting as a waveguide. Obviously, a standing wave is built by superposition of two plane waves, propagating as a monochromatic beam of 16.2 keV within the film of 15.4 nm thickness. The authors detected a refracted beam at 10.2 keV for an incident angle of 0.18° and an exit angle of 0.0433° in accord with Equation 1.83. The width of this peak was about 0.6 keV for a beam with a divergence of 0.1° . The authors suggested the use of a silicon wafer as a refractive monochromator and the application of cutoff and refracted beams for angular calibration of the experimental setup [82].

REFERENCES

1. Franks, A. (1997). The First Hundred Years. In: Michette, A. and Pfauntsch, S. (editors) *X-Rays*, John Wiley & Sons: New York, pp. 1–19.
2. Friedrich, W., Knipping, P., and von Laue, M. (1912). *Interferenzerscheinungen bei Röntgenstrahlen*, Bayerische Akademie der Wissenschaften zu München, Sitzungsberichte math.-phys. Kl., p. 303–322. Reprinted (1913): *Annalen der Physik* **41**, 971–988.
3. Moseley, H.G.J. (1913). The high frequency spectra of the elements. *Phil. Mag.*, **26**, 1024–1034; and Moseley, H.G.J. (1914). The high frequency spectra of the elements. Part II. *Phil. Mag.*, **27**, 703–713.
4. Long, J. (1997). X-ray microanalysis. In: Michette, A. and Pfauntsch, S. (editors) *X-Rays*, John Wiley & Sons: New York, pp. 21–40.
5. Barkla, C.G. (1905). Polarised Röntgen radiation. *Philos. Trans. R. Soc. London*, **A204**, 467–480.
6. Barkla, C.G. (1911). The spectra of the fluorescent Röntgen radiations. *Phil. Mag.*, **22**, 396–412.
7. Compton, A.H. (1923). The total reflection of X-rays. *Phil. Mag.*, **45**, 1121–1131.
8. Klockenkämper, R. (1997), *Total-Reflection X-Ray Fluorescence Analysis*, 1st ed., John Wiley & Sons, Inc., New York.
9. Hennig, U. (1989). *Deutsches Röntgen-Museum Remscheid-Lennep*, G. Westermann Verlag: Braunschweig, pp. 3–128.
10. Yoneda, Y. and Horiuchi, T. (1971). Optical flats for use in X-ray spectro-chemical microanalysis *Rev. Sci. Instrum.*, **42**, 1069–1070.
11. Wobrauschek, P. (1975). *Totalreflexions-Röntgenfluoreszenzanalyse*, PhD thesis. Available from: Atominstytut der Österreichischen Universitäten, Technical University of Vienna, Austria.

12. Aiginger, H. and Wobrauschek, P. (1974). A method for quantitative X-ray fluorescence analysis in the nanogram region. *Nucl. Instr. Meth.*, **114**, 157–158.
13. Aiginger, H. and Wobrauschek, P. (1975). Total-reflection X-ray fluorescence spectrometric determination of elements in nanogram amounts. *Anal. Chem.*, **47**, 852–855.
14. Knoth, J. and Schwenke, H. (1978). An X-ray fluorescence spectrometer with totally reflecting sample support for trace analysis at the ppb level. *Fresenius Z. Anal. Chem.*, **291**, 200–204.
15. Schwenke, H. and Knoth, J. (1982). A highly sensitive energy-dispersive X-ray spectrometer with multiple total reflection of the exciting beam. *Nucl. Instr. Meth.*, **193**, 239–243.
16. Boumans, P.W.J.M. and Klockenkämper, R. editors (1989). Total reflection X-ray fluorescence spectrometry. *Spectrochim. Acta*, **44B**, 433–549.
17. Boumans, P.W.J.M., Wobrauschek, P., and Aiginger, H. editors (1991). Total reflection X-ray fluorescence spectrometry: Proceedings *Spectrochim. Acta* **46B**, 1313–1436.
18. Boumans, P.W.J.M. and Prange, A. editors (1993). Total reflection X-ray fluorescence spectrometry: Proceedings *Spectrochim. Acta*, **48B**, 107–299.
19. Taniguchi K. editor (1995). *Adv. X-Ray Chem. Anal. Jpn.*, **26s**, 1–206.
20. de Boer, D.K.G. and Klockenkämper, R. editors (1997). Total reflection X-ray fluorescence analysis: 6th conference on total reflection X-ray fluorescence analysis and related methods. *Spectrochim. Acta*, **52B**, 795–1072.
21. Wobrauschek, P. editor (1999). *Spectrochim. Acta*, **54B**, 1383–1544.
22. Strelci, C. and Wobrauschek, P. editors (2001). *Spectrochim. Acta*, **56B**, 2003–2336.
23. de Carvalho, M.L. editor (2003). *Spectrochim. Acta*, **58B**, 2023–2260.
24. Gohshi, Y., Kawai, J., and Taniguchi, K. editors (2004). *Spectrochim. Acta*, **59B**, 1047–1334.
25. Zaray, Gy. and Ovari, M. editors (2006). *Spectrochim. Acta*, **61B**, 1081–1239.
26. Pepponi, G. editor (2008). *Spectrochim. Acta*, **63B**, 1349–1510.
27. Boman, J. editor (2010). *Spectrochim. Acta*, **65B**, 427–508.
28. Becker, R.S., Golovchenko, J.A., and Patel, J.R. (1983). X-ray evanescent-wave absorption and emission. *Phys. Rev. Lett.*, **50**, 153–156.
29. Iida, A., Yoshinaga, A., Sakurai, K., and Gohshi, Y. (1986). Synchrotron radiation excited X-ray fluorescence analysis using total reflection of X-rays. *Anal. Chem.*, **58**, 394–397.
30. Klockenkämper, R., Knoth, J., Prange, A., and Schwenke, H. (1992). Total-reflection X-ray fluorescence spectroscopy. *Anal. Chem.*, **64**, 1115A–1123A.
31. Klockenkämper, R. (1991). Totalreflexions-Röntgenfluoreszenzanalyse. In: Günzler, H. et al., (editors) *Analytiker Taschenbuch*, Vol. 10, Springer-Verlag: Berlin; Band 111–152.
32. von Bohlen, A. (2009). Total reflection X-ray fluorescence and grazing incidence X-ray spectrometry – Tools for micro- and surface analysis: a review. *Spectrochim. Acta*, **64B**, 821–832.
33. Alov, N.V. (2011). Total reflection X-ray fluorescence analysis: physical foundations and analytical application (A review). *Inorganic Materials*, **47**, 1487–1499.

34. Wobrauschek, P. (2007). Total reflection X-ray fluorescence analysis: a review. *X-Ray Spectrom.*, **36**, 289–300.
35. Kregsamer, P., Strel, C., and Wobrauschek, P. (2002). Total reflection X-ray fluorescence. In: Van Grieken, R. and Markowicz, A. (editors) *Handbook of X-Ray Spectrometry*, 2nd ed., Marcel Dekker, pp. 559–602.
36. Fabry, L., Pahlke, S., and Beckhoff, B. (2011). Total-reflection X-ray fluorescence (TXRF) analysis. In: Friedbacher, G. and Bubert, H. (editors) *Surface and Thin Film Analysis*, 2nd ed., Wiley-VCH, pp. 267–292.
37. Mori, Y. (2004). Total-reflection X-ray fluorescence for semiconductors and thin films. In: Tsuji, K., Injuk, J., and Van Grieken, R. (editors) *X-Ray Spectrometry: Recent Technological Advances*, John Wiley & Sons: New York, pp. 517–533.
38. Meirer, F., Singh, A., Pepponi, G., Strel, C., Homma, T., and Pianetta, P. (2010). Synchrotron radiation-induced total reflection X-ray fluorescence analysis. *Trends Anal. Chem.*, **29**, 479–496.
39. Strel, C., Wobrauschek, P., Meirer, F., and Pepponi, G. (2008). Synchrotron radiation induced TXRF. *J. Anal. At. Spectrom.*, **23**, 792–798.
40. von Bohlen, A., Krämer, M., Sternemann, C., and Paulus, M. (2009). The influence of X-ray coherence length on TXRF and XSW and the characterization of nanoparticles observed under grazing incidence of X-rays. *J. Anal. At. Spectrom.*, **24**, 792–800.
41. von Bohlen, A., Brücher, M., Holland, B., Wagner, R., and Hergenröder, R. (2010). X-ray standing waves and scanning electron microscopy – Energy dispersive X-ray emission spectroscopy study of gold nanoparticles. *Spectrochim. Acta*, **65B**, 409–414.
42. Szoboszlai, N., Polgari, Z., Mihucz, V., and Zaray, G. (2009). Recent trends in total reflection X-ray fluorescence spectrometry for biological applications. *Analytica Chimica Acta*, **633**, 1–18.
43. Schmeling, M. and Van Grieken, R. (2002). Sample preparation for X-ray fluorescence. In: Van Grieken, R. and Markowicz, A. (editors) *Handbook of X-Ray Spectrometry*, 2nd ed., Marcel Dekker, pp. 933–976.
44. Kunimura, S., Watanabe, D., and Kawai, J. (2009). Optimization of a glancing angle for simultaneous trace element analysis by using a portable total reflection X-ray fluorescence spectrometer. *Spectrochim. Acta*, **64B**, 288–290.
45. Kiessig, H. (1931). Untersuchungen zur Totalreflexion von Röntgenstrahlen. *Ann. Phys.*, **10**, 715–768.
46. Du Mond, J. and Youtz, J.P. (1940). An X-ray method of determining rates of diffusion in the solid state. *J. Appl. Phys.*, **11**, 357–365.
47. National Institute of Standards and Technology (2010). The NIST Reference on Constants, Units, and Uncertainty. <http://physics.nist.gov/cuu/Constants/>
48. Bertin, E.P. (1975). *Principles and Practice of Quantitative X-ray Fluorescence Analysis*, 2nd ed., Plenum Press: New York.
49. Jenkins, R., Manne, R., Robin, R., and Senemaud, C. (1991). IUPAC - Nomenclature system for X-ray spectroscopy. *X-Ray Spectrom.*, **20**, 149–155.
50. Tertian, R. and Claisse, F. (1982). *Principles of Quantitative X-ray Fluorescence Analysis*, Heyden: London.
51. Elder, F.R., Gurewitsch, A.M., Langmuir, R.V., and Pollock, H.C. (1947). Radiation from Electrons in a Synchrotron. *Phys. Rev.*, **71**, 829–830.

52. http://asd.gsfc.nasa.gov/Volker.Beckmann/school/download/Longair_Radiation2.pdf
53. Wille, K. (1992). *Physik der Teilchenbeschleuniger und Synchrotronstrahlungsquellen*, Teubner Studienbücher, Physik: Stuttgart.
54. Schwinger, J. (1949). On the classical radiation of accelerated electrons. *Phys. Rev.*, **75**, 1912–1925.
55. Munro, I. (1997). The First Hundred Years. In: Michette, A. and Pfauntsch, S. (editors) *X-Rays*, John Wiley & Sons: New York, pp. 131–154.
56. Als-Nielsen, J. and Mc Morrow, D. (2001). *Elements of Modern X-Ray Physics*, 4th reprint 2010, John Wiley & Sons, Ltd.: New York.
57. Author collective (1986). Vaughan, D. (editor) *X-ray Data Booklet*. 1st ed., Lawrence Berkeley Laboratory: Berkeley; third edition (2009), editor A.C. Thompson.
58. http://en.wikipedia.org/wiki/Synchrotron_radiation; August 2014, Wikimedia Foundation, Inc., USA, October 2014
59. http://www.ira.inaf.it/~ddallaca/P-Rad_3.pdf; 2014, Daniele Dallacasa, INAF - ISTITUTO DI RADIOASTRONOMIA, Bologna, Italy, October 2014
60. <http://www.lightsources.org/2013>, Management Board Lightsources.org, October 2014
61. <http://www.cxro.lbl.gov/A> U.S. Department of Energy National Laboratory Operated by the University of California 2014, X-ray Data Base, 2014.
62. Longair, M.S. (1981). *High Energy Astrophysics*, 3rd ed. 2011, Cambridge University Press: Cambridge, 440 pages.
63. Weis, T., Bergers, U., Friedl, J., Hartmann, P., Heine, R., Huck, H., Kettler, J. Kopitzki, O., Schirmer, D., Schmidt, G., and Wille, K. (2006). *Status of the 1.5 GeV Synchrotron Light Source DELTA and related Accelerator Physics Activities*. In: *RuPAC*, Novosibirsk.
64. <http://www.delta.tu-dortmund.de>; 2014, Technische Universität Dortmund, 44227 Dortmund, Germany, October 2014
65. Jackson, J.D. (1982). *Klassische Elektrodynamik*, 2nd ed., de Gruyter: Berlin, New York.
66. Hoffmann, A. (1986) *Theory of Synchrotron Radiation*, SSRL (ACD-note 38).
67. Mills, D.M., Helliwell, J.R., Kwick, A., Ohta, T., Robinson, I.A., and Authier, A. (2005). Report on the Working Group on Synchrotron Radiation Nomenclature – brightness, spectral brightness or brilliance. *J. Synchrotron Rad.*, **12**, 385.
68. Schirmer, D. (2005). *Synchrotron Radiation Sources at DELTA*, University of Dortmund, DELTA: Int. Rep. 001-05.
69. en.wikipedia.org/wiki/Planck's_law
70. Williams, K.L. (1987). *An Introduction to X-Ray Spectrometry*, Allen & Unwin: London.
71. Krieger, H. and Petzold, W. (1989). *Strahlenphysik, Dosimetrie und Strahlenschutz*, Bd. 2, Teubner: Stuttgart.
72. Woldseth, R. (1973). *All you ever wanted to know about X-Ray Energy Spectrometry*, Kevelex Corp.: Burlingame, California.
73. Veigele, W.J. (1973). *Atomic Data Tables*, **5**, 51–111.
74. James, R.W. (1967). *The Optical Principles of the Diffraction of X-rays*, Cornell University Press: Ithaca, NY.

75. Stanglmeier, F. (1990). *Bestimmung der dispersiven Korrektur $f(E)$ zum Atomformfaktor aus der Totalreflexion von Röntgenstrahlen*, Forschungszentrum Jülich: Berichte Nr. 2346. (Dissertation TH Aachen).
76. Blochin, M.A. (1957). *Physik der Röntgenstrahlen*, VEB Verlag Technik: Berlin.
77. Born, M. and Wolf, E. (1959). *Principles of Optics*, 6th ed., Pergamon Press: London, p. 36–51.
78. Hayashi, K., Kawai, J., Moriyama, Y., Horiuchi, T., and Matsushige, K. (1999). Refracted X-rays propagating near the surface under grazing incidence condition. *Spectrochim. Acta*, **B54**, 227–230.
79. Yoneda, Y. (1963). Anomalous surface reflection of X rays. *Phys. Rev.*, **131**, 2010–2013.
80. Nigam, A.N. (1965). Origin of anomalous surface reflection of X rays. *Phys. Rev.*, **138**, A1189–A1191.
81. Ebel, H., Svagera, R., and Ebel, M.F. (2001). X-ray waveguide phenomenon in thin layers under grazing incidence conditions. *X-Ray Spectrom.*, **30**, 180–185.
82. Ebel, H., Streli, C., Pepponi, G., and Wobrauschek, P. (2001). Energy dispersion of X-ray continua in the energy range 8 keV to 16 keV by refraction on Si wafers. *Spectrochim. Acta*, **B56**, 2045–2048.
83. Ebel, H. (2002). Quantification of the monochromatic photon flux of refractive X-ray monochromators in the energy range from 10 to 30 keV. *X-Ray Spectrom.*, **31**, 368–372.